Dynamic Response of the Fluid Mud to a Tropical Storm

Ge, Jianzhong ; Chen, Changsheng; Wang, Zhengbing ; Ke, Keteng; Yi, Jinxu; Ding, Ping Xing

DOI
10.1029/2019JC015419

Publication date
2020

Document Version
Accepted author manuscript

Published in
Journal Of Geophysical Research-Oceans

Citation (APA)
Ge, J., Chen, C., Wang, Z., Ke, K., Yi, J., & Ding, P. X. (2020). Dynamic Response of the Fluid Mud to a Tropical Storm. *Journal Of Geophysical Research-Oceans*, *125*(3), Article e2019JC015419. https://doi.org/10.1029/2019JC015419

Dynamic Response of the Fluid Mud to a Tropical Storm

Jianzhong Ge[*1,2], Changsheng Chen[3], Zheng Bing Wang[4,5], Keteng Ke[1,6], Jinxu Yi[1], Pingxing Ding[1]

[1]State Key Laboratory of Estuarine and Coastal Research, East China Normal University, Shanghai, China, 200062

[2]Institute of Eco-Chongming (IEC)， No.20 Cuiniao Road, Chen Jiazhen, Shanghai, China, 202162

[3]School for Marine Science and Technology, University of Massachusetts-Dartmouth, New Bedford, MA 02744, United States

[4]Faculty of Civil Engineering and Geosciences, Delft University of Technology, 2628 CN Delft, The Netherlands

[5]Deltares, 2600 MH Delft, The Netherlands

[6]Shanghai Investigation, Design & Research Institute, Shanghai, China, 200050

Corresponding author: Dr. Jianzhong Ge (jzge@sklec.ecnu.edu.cn)

Key Points:

- A strong fluid mud (FM) formed during the passage of a tropical storm.
- Numerical model revealed storm increased stratification that initially triggered the massive formation of FM.
- Model indicated FM was sustained and transported by saltwater intrusion, and it finally broke down in subsequent strong-mixing spring tide.

Abstract

Fluid mud (FM) is a unique sedimentary feature in high-turbidity estuaries that makes a rapid contribution to morphodynamics. Insufficient field measurements and monitoring leads to deficient understanding of the formation, transport, and breakdown of FM under extreme weather conditions is not well understood. A field survey was conducted in the period of turbidity maximum in the Changjiang Estuary, just after Typhoon Haikui. The measurements captured the formation of FM beneath the suspended layer, particularly around the lower reach of the North Passage. The thickness of the observed FM gradually decreased landward along the channel, with the maximum value of ~0.9 m. This feature of the observed storm-induced FM was determined by the simulation using the Finite-Volume Community Ocean Model (FVCOM). The results indicated that the initial appearance of the FM was the result of typhoon-intensified stratification in the outlet region. The subsequent landward propagation of the FM was driven by the combined effects of a FM-induced mud-surface pressure gradient force and the saltwater intrusion near the bottom. The weak mixing during the following neap tide period sustained the FM as it rapidly extended into the middle region of the North Passage. This produced a large velocity shear at the interface of the FM and the upper suspension layer, increasing entrainment from the FM to the upper suspension layer. The FM weakened and finally broke down in the subsequent spring tidal period as a result of increased tidal mixing.

Plain Language Summary

The continuum from large river to estuary is generally a high turbidity environment and frequently produces highly concentrated benthic sediment suspensions, i.e., fluid mud (FM). The FM is a sediment feature, with concentration mostly in the range of 10 to >100 g/L. It is difficult to track its movement and breakdown. The response of the FM to extreme atmospheric and oceanic conditions is therefore not well understood. In this study, a comprehensive field campaign identified the large-scale formation of the FM in the Changjiang Estuary, after a severe tropical storm attacked. The full life cycle of FM in this passage cannot, however, be determined through the field observation alone. A two-layer FM model was developed to achieve this goal. Model experiments suggested that key physical factor was the stratification as a result of the typhoon-enhanced saltwater intrusion. This led to the formation of FM in the near-bottom layer. After formation, the FM extended onshore along the shipping channel under the influence of ambient saltwater intrusion. The FM was constrained in the benthic layer as a consequence of the weak mixing from the intrusion physics. The breakdown of the FM was governed by enhanced tidal mixing in the subsequent spring tide.

1 Introduction

Fluid mud (FM), referring to concentrated benthic suspension, is a distinctive sediment feature in the high-turbidity environment of coastal and estuarine regions, such as the Mississippi River estuary, Amazon River delta, Jiaojiang river mouth, Changjiang Estuary, etc. (Winterwerp, 1999; Winterwerp and Van Kesteren, 2004; Guan et al., 2005; Corbett et al., 2007; Xie et al., 2010; Wan et al., 2014). The FM generally forms an intermittent buffer between an upper relatively low-concentration sediment suspension layer and a lower consolidated bed layer. It is an active sediment source for the upper suspension layer through an entrainment process and for the bed layer through sedimentation. It is also a sediment sink from the upper layer by deposition and from the bed layer by erosion (Winterwerp and Van Kesteren, 2004; Yang et al., 2015; Ge et al., 2018). The FM can cause very fast sedimentation rates, contributing directly to morphological processes in high-turbidity waters.

It is quite difficult to detect the existence of the FM, and even more difficult to track its movement and breakdown. The typical sediment concentration within the FM is in the range of 10 to >100 g/L. The FM can sustain a very thin vertical thickness, which is not easily resolved in ship-board observations. Ge et al. (2018) developed a sophisticated monitoring system; a bottom-mounted tripod equipped with various sensors. This system successfully captured the formation and variation of thin FM layers in the Changjiang River Estuary, and hence identified the associated hydro and sediment dynamics.

The FM formation process was simulated using a one-dimensional vertical (1DV) model (Winterwerp, 2011, Ge et al., 2018). However, the FM transport is a three-dimensional (3D) dynamic problem that cannot be fully resolved by a 1DV model based on limited/sparse site observations. Developing a 3D model is required to examine various rheological behaviors and to replicate the FM, or a FM layer, which are observed in either laboratory-scale experiments or realistic estuarine conditions (e.g., Wang et al., 1992; Le Hir et al., 2000; Guan et al., 2005; Knoch and Malcherec, 2011). The most common 3D FM models discretized the vertical into a two-layer system consisting of water column and fluid mud (Wang et al., 2008; Yang et al., 2015). These models are capable of resolving FM from the laboratory-scale experiments (Knoch and Malcherec, 2011; Yang et al., 2015)) and an idealized estuary (Hsu et al., 2009), but only a few have reproduced the FM within or around a real river estuary (Guan et al., 2005). Both laboratory experiments and numerical simulations were mainly focused on the hydrodynamics responsible for the FM formation, which included tidal currents, surface waves and current-wave interactions (Winterwerp et al., 2002).

During the calm weather, the thickness of the FM was observed with a tidally-averaged mean value of < 0.3 m around the Changjiang Estuary and its adjacent coastal regions (Yang et al., 2015; Ge et al., 2018). Under some deposition events, much greater FMs could occur, with evidences recorded in previous studies over the Waipaoa River shelf, northern California shelf, Eel River shelf, Louisiana shelf, and Elwha River (Hale et al., 2014; Ogston., 2000; Traykovski et al., 2000, 2015; Eidam et al., 2019). However, the FM features under extreme weather conditions, particularly storm events, have not been well-documented, which are a considerable challenge for both monitoring and modelling. A storm can cause rapid changes in currents and surface waves. The FM is characterized with a lutocline forming ultimately from rapid settling flux, suggesting that the FM could not form under strong vertical mixing conditions. The storm can produce a strong horizontal advection, which can push a newly formed FM into a remote area from its origin to yield the appearance of the FM over there. The FM may be scattered over a wide area and may vary greatly over time. Under severe weather conditions, the formation and movement of the FM can produce substantial morphological changes, which can directly influence estuarine mixing, stratification and currents. The formation, transport, and breakdown of the FM involves complex 3D dynamics that cannot symmetrically be understood only through observations and 1DV numerical simulation.

To investigate the formation and transport dynamics of the FM in a high-turbidity estuarine environment under extreme weather conditions, we had designed a rapid-response field measurement plan for the Changjiang River Estuary. Under this plan we developed a monitoring network with various instruments and sensors that is capable to measure the spatial distribution of the sediment, water temperature and salinity as well as currents in and around the estuarine tidal channel over a short period of a few hours or up to one day after a storm passed. This network measurements were made after Typhoon Haikui, which successfully captured a significant FM in the high-turbidity zone of the Changjiang River Estuary. The observational data was first analyzed to synthesize the observed features of this FM and then a two-layer FM sediment model, which was coupled with the latest version of the three-dimensional Finite-Volume Community Ocean Model (FVCOM), was used to examine the dynamics of the formation and transport processes of the observed FM.

This paper is organized as follows. The study sites, measurement configuration and model development are described in Section 2. The FM observations and the corresponding physical processes are presented and discussed in Section 3. The model-simulated post-typhoon dynamics of formation and transport of the FM in the Changjiang Estuary are given in Section 4. The physical mechanism and processes as well as some critical issues are discussed in Section 5. The major finding and conclusions are summarized in section 6.

2 Study site and Measurement

2.1 The study site and Typhoon Haikui

The Changjiang River Estuary (Fig. 1a) is a high-turbidity estuary connecting to the inner shelf of the East China Sea, with abundant sediment supply from the upstream region (Chen et al., 1999; Shen et al., 2012). Although as a consequence of numerous upstream damming activities the sediment discharge has significantly decreased from ~4.0×10^8 tons/year in 1980s to ~1.0×10^8 tons/year in 2000s (Yang et al., 2011), this estuary is still characterized by strong turbidity maximum (an enlarged view is shown in Fig. 1b) (Wan and Wang, 2017; Li et al., 2017). The formation of FM is often observed in the estuarine channels, particularly around the high-water slack, *i.e.* from late flood to early ebb period (Wan et al., 2014; Ge et al., 2018).

The North Passage is the major shipping channel in the Changjiang River Estuary. Two dikes and dozens of groynes were constructed over the neighboring shoals to enhance the shipping capacity (Ge et al., 2012; Pu et al., 2015). This passage is fully constrained in turbidity maximum with turbulent mixing varying from well-mixed to strongly stratified. It is the primary meeting place of freshwater discharge and saline water intrusion and suffered from sediment accumulation(Chen et al., 2003; Chen et al., 2008, Xue et al., 2009, Pu et al., 2015; Wan and Wang, 2017; Li et al., 2017).

Typhoon Haikui originated southeast of Iwo Jima as a tropical depression, and then grew to a tropical cyclone during late July and early August, 2012. It was upgraded to a Category-I typhoon on August 6, and made the landfall over the Xiangshan region in Zhejiang Province, China on August 8 (Fig. 1a). In the Changjiang River Estuary region, the typhoon caused serious coastal flooding in the coastal region from Shanghai City to Zhejiang Province.

2.2 Field measurement

One day after the typhoon passed, a field survey was conducted around the mouth of the Changjiang River Estuary (Fig. 1b). A series of cross-estuarine sections were selected near the North Passage navigation channel, including CS9, CS2, CSW, CS3, CS7, CS4, and CS10. There were two or three ship-anchored sites on each section. Suffix *S* and suffix *N* referred to the sites located on the southern and northern sides of the navigation channel, respectively, while suffix *M* refers to a site located exactly in the middle of the navigation channel. This navigational channel is one of the busiest shipping lanes in the world. For safety, the *M*-sites were sampled with lower frequency than the *S*- and *N*-sites.

The survey started on August 12, just one day after the typhoon all-clear was declared, and ended on August 18. This field campaign period covered a typical spring tidal (August 17-18), neap tidal (August 12-13), and spring-neap transition cycle (August 14-15). To resolve the spatial distribution of sediment concentrations, a total of 10 vessels participated and the measurements were made simultaneously on all vessels along the main channel of the North Passage (red dots in Fig. 1b). The vessels were all equipped with the same types of instruments and sensors, including current meters and water sampling equipment. The Acoustic Doppler Current Profiler (ADCP) with acoustic sensor frequency of 600KHz were used to measure the water current profile. The vertical sampling resolution of ADCP was specified to be 0.5 m. The salinity, and suspended sediment concentration (SSC) were directly sampled at 6 depths in the water column. These vertical samples were located at relative depths of 5%, 20%, 40%, 60%, 80%, and 95% of the total instantaneous water depth. Three wind-wave buoys were deployed at Niu Pi Jiao (NPJ), Chang Jiang Kou (CJK), and Nan Cao Dong (NCD). These buoys functioned as operational wave platforms: significant wave height, peak wave period and wave direction were recorded at hourly time intervals during the typhoon passage (blue dots in Fig. 1).

Teledyne Odom Echotrac MK III with two sonar sensors of high-frequency (220 kHz) and low-frequency (33 kHz) transducers were set up to measure the water depth along the main channel. This measurement was conducted in just one day of August 12. The measurement uncertainties were 0.1 m at 33 KHz and 0.01m at 220 KHz, respectively. The depth differences between the high-frequency and low-frequency sonars were used to estimate the thickness of the FM along the main channel. Since the depth measurements of both acoustic sensors mainly depended on the density gradient near the interface between water and FM, a laboratory experiment with the field-collected FM was conducted to calibrate the sound speed and other parameters for sonar sensors. An additional Stema Systems RheoTune probe was used to measure the density profile in the fluid mud layer for this ground-truthing experiment. This helped us determine the density threshold for acoustic reflectance of high- and low-frequency sensor.

Since the FM was formed originally from suspended and bed sediments, it was highly related with bed properties. The seabed sediments around the Changjiang Estuary were sampled simultaneously with the hydrodynamic measurements, starting from August 12. The sample resolution was relatively higher in the North Passage than in the South Passage, North Channel and other adjacent regions (black dots in Fig. 1b). These sediment samples were used to measure the grain size distribution. In particular, the median grain size (d_{50}) was measured using the particle laser diffraction method with Beckman Coulter LS13-320.

3 Observational results

3.1 Hydrographic observation

We found that all sites, whether in the northern, southern or middle areas of the North Passage, exhibited similar temporal patterns (Fig 2). CSWM, a site located in the middle area of the North Passage, was chosen to quantify the physics in the suspension layer. This is a tidally-dominant passage with relatively strong vertical velocity shears throughout the water column (Fig.2a). During the spring tide, the maximum velocity was ~3.0 m/s near the surface and ~1.9 m/s near the bottom (Fig 2a), with a surface-bottom difference of ~1.1 m/s. The tidal velocities near the surface and bottom during the neap tide were ~2.2 m/s and ~1.2 m/s, respectively (Fig. 2a). The vertical shear of the velocity was thus the same as that found during the spring tide. This strong vertical shear is relevant to vertical stratification.

The water was strongly stratified during the neap tide and vertically well-mixed during the spring tide. During the neap tide, the flow featured a dominant two-layer structure with a difference of ~180° in direction between the surface and bottom. This is evident in Fig. 2b, which shows that the water moved seaward with a flow direction of ~115° in the upper layer and landwards with a flow direction of ~290° in the lower layer. The direction difference between these two layers was ~175°. This two-layer pattern was most clear at 13:00 August 12-13:00 August 13 and 15:00-18:00 August 13. As the tidal currents intensified during the spring tide, tidal-induced vertical mixing weakened the vertical stratification and made the tidal velocity distribution nearly uniform through the water column.

The time-varying stratification was verified by the salinity measurements. The vertical profiles of salinity and SSC showed that the region was generally stratified, particularly around slack water times during the neap tide (Fig. 2c-d). At 06:00 August 13, the salinity near the bottom reached a maximum value of 29.3 PSU. During the spring tide on August 18, there was a strong tidal current near the surface (Fig. 2a). The consequent enhanced vertical shear produced strong mixing and made the water vertically well mixed (Fig. 2c).

The SSC showed a similar vertical distribution pattern to the salinity. During the neap tide, the water column was dominated mainly by low-SSC water, except for the near-bottom layer where high-SSC was observed. The observed SSC in the upper water column was in the range of 0.1 g/L to 5.6 g/L, while the SSC in the lower water column near the bottom jumped sharply to above 20.0 g/L, with the maximum value of 26.4 g/L (Fig. 2d).

The status of stratification is further estimated using the gradient Richardson number (R_i):

$$R_i = -\frac{g}{\rho_w}\frac{\partial\rho/\partial z}{[(\frac{\partial u}{\partial z})^2+(\frac{\partial v}{\partial z})^2]} \quad (1)$$

where ρ_w is water density considering the joint effect of salinity and SSC, $\partial\rho/\partial z$ is the density gradient, u, v are velocity components in the x-, and y-directions. The water column is considered to be stratified when R_i exceeds 0.25. Therefore $\log_{10}(Ri/0.25)$ is used as an index for the degree of stratification. Fig. 2e shows the distribution of the index and reveals that the water column experienced strong and persistent stratification during neap tide cycles on Aug 12-13, as well as in the transitional period from neap to spring on Aug 15-16. During the spring cycles, Aug 17-18, the level of stratification had rapid variations: the water column was stratified during the flood cycle and well-mixed in the ebb cycle (Fig. 2e).

Many other measurement sites and transects, including transects CS2, CS6, CS7 and CS3, showed the same pattern with the same physics (Table 1). In particular, the observed SSC rose to 45.0 g/L and greater at sites located in the middle channel of the North Passage, with high values at CS2M, CS6M, CSWM, CS3M, CS4M, and CS10M. At several sites, the SSC was found to be greater than 80.0 g/L, suggesting the existence of the FM within the navigation channel in the North Passage. By comparison, the SSC in the upper water column was small, within a general range of 0.0-5.0 g/L, and with a maximum value below 10.0 g/L. The strong vertical SSC column gradient indicated that the concentrated suspension was mainly restricted to near the bottom.

3.2 Observed FM distribution

The difference between the depths measured with the low- and high-frequency sonars was used as an indicator of the FM, or fluid mud, thickness. Using the cruise-tracking, recorded along the navigational channel, we plotted the along-channel distribution of FM thickness (Fig. 3a). To estimate the extent of the FM, we divided the shipping channel into 46 units. Each unit was about 2-3 km long and 350 m wide (the approximate width of the shipping channel). The estimated values of FM thickness were based on spatial averaging in each unit. This showed that the FM existed, with varying thickness, along the navigation channel from the entrance to the outlet of the North Passage. The thickest FM occurred around the CS4 section in the outlet region, with the maximum value of ~1.0 m at the 36~38 segment positions (Fig. 3b). A similar thickness of FM, about 0.74 m, occurred near CS2. The other sites had relatively low thickness, ranging from 0.05 to 0.23 m. This indicated that a significant FM was detected in the lower reach of the North Passage after the typhoon landfall.

The volume of FM / fluid mud was estimated, per section, based on the channel area and the thickness of FM. The volume peaks tend to correspond with the FM thickness peaks (Fig. 3b). The largest unit volumes were ~7.5×10^5 m^3 around segment-39, and ~2.5×10^5 m^3 at segment-20.

3.3 Observed bed composition

The spatial distribution of the observed sediment median grain size (d_{50}) in the North Passage and adjacent channels showed that this river mouth was mainly covered by fine sediment, with grain sizes smaller than 50 μm (Fig.4a). The upper and lower reaches of the North Passage had even smaller sediment grain sizes. Several patches were classified to 20 μm. The grain size at the centers of these patches was < 10 μm. This confirms that the North Passage provided an adequate sediment source for the FM formation. The clay content had a similar distribution to the fine sediment. Patches with smaller grain size corresponded with the high clay component (Fig. 4b).

4 Numerical model for fluid mud

4.1 The fluid mud model

To understand the life cycle behavior of the FM during and after the typhoon landfall, FVCOM was configured to simulate the relevant physical processes. FVCOM is three-dimensional (3D) unstructured-grid primitive equation ocean numerical model (Chen et al., 2003, 2006). It discretizes the horizontal space into a triangular mesh and the vertical into terrain-following coordinates. This allowed accurate geometric fitting for the complex boundaries around the river mouth, and particularly for the dikes and groynes within the North Passage. Since these were constructed near the mean sea level, leading to submergence during high water and emergence during low water, the dike-groyne algorithm was activated to better simulate water and sediment transport over the dikes and groynes (Ge et al., 2012). The latest version 4.3 of FVCOM has integrated the dynamics of sediment transport as an independent module. This has been shown to be capable of effectively modeling the cohesive sediment dynamics around the Changjiang Estuary (Ge et al., 2015).

In addition to the original hydrodynamics, sediment and dike-groyne modules, a two-layer FM model was developed and implemented within the FVCOM sediment module with an aim at resolving and simulating the FM and upper suspension in an estuary. Since the SSC was much greater in the FM than in the upper suspension layer, it is reasonable to simplify the complex dynamics to a two-layer system with FM being a thin layer at the bottom of the benthic column that is covered by low-SSC water. This simplification was used by Wang and Winterwerp (1992), and further used in Winterwerp et al. (1999, 2002) and Ge et al. (2018) within their one-dimensional vertical (1DV) or two-layer modeling experiments. Computationally, the model then had three layers: suspension, FM, and sea bed (Ge et al., 2018). The suspension layer represented the sediment dynamics for low-to-medium SSC, the FM was placed between the suspension and bed layers, with a constant sediment concentration and a varying thickness. The sea bed layer provided the major source and sink for the suspension and FM layers through vertical sediment exchange.

Winterwerp (1999) outlined a basic three-dimensional framework for FM flow and its related dynamics (Fig. 5). Multiple physical processes occur at the interface between the suspension and FM layers and between the FM and sea bed layers. The sediment deposition from the suspension layer and erosion from the bed layer jointly function as sources contributing to the formation of the FM. The entrainment process from the FM to the suspension layer and the dewatering effect from the FM to the sea bed are sinks, leading to the breakdown of the FM (Fig. 5). These physical source/sink processes nonlinearly interact in space and time, leading to varying thickness of the FM. The FM also acts as a drag force at the suspension-FM interface. The erosion and deposition processes are controlled by the turbulent kinetic energy in the water column and the shear stress at the bottom produced by the wave-current interaction.

In FVCOM the sediment dynamics within the upper suspension layer are controlled by advection, diffusion, and particle settling. The governing equations in the water column, following Chen et al. (2013), are

$$\frac{\partial C}{\partial t}+\frac{\partial uC}{\partial x}+\frac{\partial vC}{\partial y}+\frac{\partial (w-w_s)C}{\partial z}=\frac{\partial}{\partial x}\left(A_H\frac{\partial C}{\partial x}\right)+\frac{\partial}{\partial y}\left(A_H\frac{\partial C}{\partial y}\right)+\frac{\partial}{\partial z}(K_h\frac{\partial C}{\partial z}) \quad (2)$$

where x, y, and z are the Cartesian coordinates; u, v, and w are the eastward, northward and upward components of water velocity; C is the sediment concentration; w_s is the settling velocity of sediment particles; A_H and K_h are horizontal and vertical eddy diffusion coefficients.

The boundary conditions at the water surface and near the sea bed are specified as

$$w_sC+\left(K_h\frac{\partial C}{\partial z}\right)=0, at\ z=\zeta, \quad (3)$$

$$w_sC+\left(K_h\frac{\partial C}{\partial z}\right)=ERO,\ at\ z=-H+\Delta z/2. \quad (4)$$

where ζ indicates the sea surface elevation and ERO represents the eroded sediment amount through the water-seabed interface. H is the water depth. Δz is the thickness of bottom discretized layer. The bottom boundary is configured a bit above bed to avoid $K_h=0$ at the bed surface.

When no FM is generated or transported, the sediment dynamics can be described using Eqs. 2-4. In the vertical direction, erosion and deposition are the two major physical processes at the interface. When a FM layer is present, the erosion term in Eq. 4 is replaced by the entrainment term from the FM layer.

When the FM occurs, the governing equations of the FM formation, transport and breakdown are as presented in Wang and Winterwerp (1992):

$$\frac{\partial d_m}{\partial t}+\frac{\partial u_m d_m}{\partial x}+\frac{\partial v_m d_m}{\partial y}=\frac{1}{c_m}\frac{dm}{dt} \quad (5)$$

$$\frac{\partial u_m}{\partial t}+u_m\frac{\partial u_m}{\partial x}+v_m\frac{\partial u_m}{\partial y}+g\frac{\rho_m-\rho}{\rho_m}\frac{\partial \eta_m}{\partial x}-\Omega v_m+\frac{1}{\rho_m d_m}(\tau_{bx}-\tau_{sx})=-\frac{1}{\rho_m}\rho g\frac{\partial \eta}{\partial x} \quad (6)$$

$$\frac{\partial v_m}{\partial t}+u_m\frac{\partial v_m}{\partial x}+v_m\frac{\partial v_m}{\partial y}+g\frac{\rho_m-\rho}{\rho_m}\frac{\partial \eta_m}{\partial y}-\Omega v_m+\frac{1}{\rho_m d_m}(\tau_{by}-\tau_{sy})=-\frac{1}{\rho_m}\rho g\frac{\partial \eta}{\partial y} \quad (7)$$

where t is time, $d_m$is the thickness of the FM layer, u_m and v_m are the eastward and northward components of the FM' horizontal velocity, respectively; $c_m$is the sediment concentration within the FM, which is constant both in height and time; m is the mass of sediment in a unit area; ρ_m is the bulk density of FM; ρ is the density of suspension in the upper layer; Ω is the Coriolis force acceleration coefficient; $\tau_{bx}$and τ_{by} are the shear stresses at the FM-bed interface in the x- and y-directions, respectively; τ_{sx} and τ_{sy} are the shear stresses at the suspension-FM interface in the x- and y-directions, respectively; $\eta_m$is the elevation of the FM; and η is the surface elevation of the suspension layer.

The horizontal movement of the FM is affected by multiple processes, including the shear stress on the FM-bed interface (τ_b) and that on the water-FM interface (τ_s), and the barotropic pressure gradient force due to the FM surface elevation (η_m) and sea surface elevation (η).

The shear stress at the FM-bed interface is calculated by:

$$\begin{pmatrix}\tau_{bx}\\ \tau_{by}\end{pmatrix} = \begin{pmatrix}u_m\\ v_m\end{pmatrix}\frac{\tau_m}{\sqrt{u_m^2+v_m^2}}, \quad (8)$$

and

$$\tau_m = \tau_B + \frac{f_m \rho_m}{8}(u_m^2 + v_m^2) \quad (9)$$

where f_m is the friction coefficient between FM layer and sea bed; $\tau_B$is the Bingham-yield strength for the transitional behavior from the Newtonian to non-Newtonian FM, which is set to 0.2 N/m^2;

The shear stress at the interface between FM and suspension layer is determined by:

$$\begin{pmatrix}\tau_{sx}\\ \tau_{sy}\end{pmatrix} = \begin{pmatrix}\Delta u\\ \Delta v\end{pmatrix}\frac{f_s \rho\sqrt{\Delta u^2+\Delta v^2}}{8}, \quad (10)$$

where f_s is the friction coefficient between the FM and the upper suspension layers; u and v are the x- and y-components of the horizontal velocity in the suspension layer, respectively; Δu and Δv are the velocity differences between the upper suspension and FM layers, respectively, and are given by

$$\Delta u = u - u_m, \quad (11)$$

$$\Delta v = v - v_m. \quad (12)$$

$\frac{1}{c_m}\frac{dm}{dt}$, the right-hand term in Eq. 5, is balanced by source and sink masses as

$$\frac{dm}{dt} = Settling - Entrainment + Erosion - Dewatering \quad (13)$$

where the $Settling$ and $Erosion$ are the source terms contributing on the formation of the FM, and $Entrainment$ and $Dewatering$ act like a sink term for the breakdown effect for the FM.

The $Settling$ is the sediment deposition from the bottom layer of the suspension layer to the FM, which is determined as

$$Settling = H\left(\frac{\tau_{dm}-\tau_s}{\tau_{dm}}\right)\omega_s C_b\left(\frac{\tau_{dm}-\tau_s}{\tau_{dm}}\right) \quad (14)$$

where $H()$ is the Heaviside function, and τ_{dm} is the critical shear stress for deposition; $C_b$is the SSC in the bottom layer of the suspension column above the FM.

Winterwerp et al. (1999) parameterized the entrainment process as:

$$Entrainment = \frac{2C_s\left(\left|u_{*,m}\right|^2 - \frac{\tau_B}{\rho_m}\right)(\vec{u}-\vec{u}_m) + C_\sigma\left(\left|u_{*,s}\right|^2 - \frac{\tau_B}{\rho_m}\right)\left|u_{*,s}\right|}{\frac{gh\Delta\rho}{\rho} + C_s(\vec{u}-\vec{u}_m)^2} C_m \quad (15)$$

in which $u_{*,s} = \sqrt[3]{u_*^3 + u_{*,m}^3}$, $u_*$is the friction velocity of the flow in the suspension layer and $u_{*,m} = f_s(u - u_m)^2$. The empirical coefficients are $C_s = 0.25$ and $C_\sigma = 0.42$. The terms in the brackets are valid only if their values are positive.

The eroded sediment amount is quantified as:

$$Erosion = H\left(\frac{\tau_b - \tau_e}{\tau_e}\right) M_e \left(\frac{\tau_b - \tau_e}{\tau_e}\right) \quad (16)$$

where M_e is the bulk erosion coefficient and τ_e is the critical shear stress for erosion. τ_b is calculated depending on the various circumstances: when the FM exists, τ_b is determined by Eq. 8. When there is no FM, τ_b is calculated through the interaction between wave and current as described in Warner et al. (2008).

The consolidation process from the FM to seabed is given as:

$$Dewatering = V_0 C_m \quad (17)$$

where V_0 is the dewatering rate.

Eqs. 2-4 govern the upper suspension layer. No matter whether FM exists or not, Eqs. 2-4 are numerically computed to determine the suspended sediment dynamics. Eqs. 5-7 are only activated when the model grid resolves the FM. The model was initialized with zero fluid-mud coverage, and ran with the inclusion of fully suspended sediment dynamics. The initial formation of fluid mud requires to meet the threshold at which the net source/sink term ($\frac{dm}{dt}$) must be positive.

Although this net source/sink term is calculated with four components (Eq. 13), when no fluid mud appears, both the entrainment and dewatering are zero. $\frac{dm}{dt}$ is determined only by settling and erosion. If $\frac{dm}{dt} > 0$, it indicates that the settling effect of suspended sediment is greater than bed erosion. That is the threshold for the initial formation of fluid mud from zero-thickness initialization. It also suggests that the fluid mud forms from rapid settling of suspended sediment, not directly from resuspension or bed erosion.

4.2 Finite-volume discrete method

Following the main framework of FVCOM, the FM model adopts non-overlapping unstructured triangular cells for horizontal discretization as described in Chen et al. (2003). Since the FM is now treated as a concentration constant and thickness-varying fluid, it can be simulated using a vertically averaged 2D model. The discretization procedure mainly adopts the 2D external mode used in the mode-splitting solver in FVCOM. The continuity equation (Eq. 5), over a control volume, is integrated numerically using the modified fourth-order Runge-Kutta time-stepping scheme. This is a multi-stage approach with second-order temporal accuracy. The same method is also used for the integration of Eqs. 6-7 to determine the vertically integrated horizontal advection, barotropic pressure gradient force resulting from the sea surface elevation, the FM elevation, and the Coriolis force. Integration of the barotropic pressure gradient force terms can be converted to a trajectory integration using Stokes'theorem. Details of the algorithm for temporal and spatial discretizations are in Chen et al. (2013). The formation, movement and breakdown of FM could be treated as a typical wet/dry process like water flooding in FVCOM. In this study, a minimum thickness of 0.05 m is used to determine the wet/dry condition for FM.

FM movement, as mentioned above, is driven by the waves and currents acting on the interface and by slope-induced gravity. The FM height varies significantly, following fast changes in the source and sink terms at the interfaces, and hence produces the FM-induced barotropic gradient force. Solving the continuity and momentum equations of the FM requires a shorter time step than that used for background hydrodynamics and the sediment model. $R_{\Delta t}$ is defined as the time-step ratio of the hydrodynamic external time step to the FM time step, which helps specification of the time step suitable for the FM dynamics.

We observed that FM was commonly generated and moving around in some particular local areas, such as the center of turbidity maximum or locations where the sediment could be easily trapped due to particular bathymetry. This means that the simulation of the FM requires a higher resolution in the regions where there is high probability of the FM occurrence. For this reason, we configured the model with two nested domains: a large domain covering the Changjiang River estuary, Hangzhou Bay, upstream Changjiang River and adjacent coastal regions, and a small refined-grid domain covering the North Passage (Fig. 6). The purpose of the two-domain nested approach is to balance the required local higher resolution with overall computational efficiency. This method had been proven effective in Ge et al. (2013).

The grid mesh in the large domain mainly followed the previous model grid used by Xue et al. (2009) and Ge et al. (2013). In this study, we have extended the grid mesh about 400 km to the upstream Datong gauge station on the lower area of the Changjiang River. The grid size of this mesh was ~5 km around the open sea boundaries (Fig. 6a), and decreased to 500 m near the river mouth (Fig. 6b). The small domain was configured with a refined mesh with the grid size as small as 100 m (Fig. 6c). The large and small domains are nested on the common-grid nesting boundary around the North Passage (blue curves and dots in Fig. 6b). The other parameters for the two domains are given in Table. 2. The small domain contained 23351 triangular cells and 12079 vertices/nodes. A mode-splitting solver was used for the simulation. In this, the currents are divided into external and internal modes that can be computed using two distinct time steps (Chen et al., 2013). The time step was 1.0 s for the external mode and 10.0 s for the internal mode in the large domain, reduced to 0.5 s and 2.5 s for the inner domain. $R_{\Delta t}$ was set to 10, which means the time step for FM was reduced to 0.05 s.

In addition, the FVCOM-SWAVE model was used to estimate full wave-current-sediment interactions. The configuration for wave computations mainly followed Qi et al. (2009) and Wu et al. (2010).

The model is driven by multiple external physical forcings. Daily freshwater discharge from the Changjiang River is considered at the upstream modeling boundary (data source: www.cjh.com.cn). A total of 10 major astronomical tidal components are specified at the lateral boundaries, including four diurnal tides (K1, O1, P1, and Q1), four semi-diurnal tides (M2, S2, N2, and K2) and two quarter-diurnal tides (M4 and MS4). The surface atmospheric forcing is provided by ERA-Interim data from the European Centre for Medium-Range Weather Forecast (ECMWF). It has 0.125° spatial resolution and 3 h temporal resolution.

4.4 Model validation and sensitivity

The model was validated for tidal elevation and currents, residual flow, salinity, and sediment concentration in previous studies (Ge et al., 2013; 2015). The same types of model-data comparisons were made in this study. Here we focus on the model-data comparison of winds, waves, and sediments.

The model was driven by tidal forcing on the open boundary in the inner shelf area of the East China Sea, by freshwater discharge from the upstream Changjiang River, and by ECMWF-derived 10-m winds and surface heat flux. We first compared the ECMWF winds with the wind records from three buoys named Chang Jiang Kou (CJK), Niu Pi Jiao (NPJ) and Nan Cao Dong (NCD) (Fig. 7a-c). The ECMWF-derived winds were a reasonable match for the observed wind variations, particularly the wind peaks during the typhoon landfall on August 8th. The wind gusts reached ~25 m/s at CJK (Fig. 7a), and ~ 20 m/s at the other two buoys (Fig. 7b-c). The root-mean-square errors at CJK, NPJ and NCD were 2.9 m/s, 1.67 m/s and 1.69 m/s, respectively. Our comparison indicated that the ECMWF-derived winds were robust, with reasonable accuracy, in the Changjiang Estuary during the survey period.

The SWAVE-simulated significant wave heights were directly compared with available wave records from the buoys. The root-mean-squared errors at CJK, NCD and NPJ were 0.52 m, 0.34 m and 0.65 m, respectively. The results showed that SWAVE not only accurately reproduced the observed significant wave heights, but also captured well wave propagation in the Changjiang Estuary during the typhoon (Fig. 7). Both SWAVE and the observations had a maximum significant wave height (H_s) of ~4.5 m on CJK (Fig. 7d) and of ~3 m on NPJ and NCD (Fig. 7e-f). The ECMWF-derived winds showed no significant difference among the three buoys, but H_s decreased significantly, by 1.5 m, from CJK to NPJ and NCD, suggesting that the typhoon produced strong swells that propagated towards the Changjiang River estuary and dissipated rapidly when reaching the dike and groyne area. The good agreement between model-simulated and observed waves made us believe that our model was capable of capturing the nonlinear wave-current interaction during the typhoon passage. Combining the water velocity data with the surface wave data, we found that the significant wave height was larger during the high tide, and lower during the low tide. This was caused by deeper water depth during high tide, which led to a weaker bottom friction for waves. It is beneficial to the wave propagation during the high tide. During the low tide, the shallower depth caused larger friction, which suppress the wave propagation.

Since the two-layer model characterizes the whole water column through two parts, upper low-SSC suspension and lower fluid mud. For the fluid mud layer, it is described as constant concentration mud column. It is unable to directly simulate the mud concentration. Therefore, to assess the model, we make the model-data comparison for upper suspended sediment concentration and FM thickness separately.

The sediment model was validated by Ge et al. (2015) through direct comparisons of sediment concentrations in the suspension layer. In this study, the comparison was focused on the FM between the suspension and seabed layers. The model-simulated and observed sediment concentrations were in good agreement at the different measurement depths over the spring-neap tide (Fig. 8). The model successfully reproduced the low-SSC region at NGN4S (Fig. 8j-l), and the high-SSC turbidity maxima at CS3S (Fig. 8a-c), CSWN (Fig. 8d-f) and CS7S (Fig. 8g-i). The model nicely resolved the SSC variation in the upper column above the middle depth. However, it failed to capture some sudden peaks near the bottom. For example, the SSC records showed a rapid SSC increase at CSWN (Fig. 8f) during the neap tide and at CS7S during the transition period (Fig. 8i). These SSC peaks had the same magnitude as those found during the spring tide and were probably caused by either mixing effect between the FM and the suspension layer or oscillations of the FM surface. This near-bottom area of the upper suspension column was affected by the lower fluid mud, leading to greater SSC in the bottom region of suspension column. This feature, however, was not included in the model. In the numerical model, the upper suspension was calculated through relatively low-SSC sediment dynamics. That is the reason the model was unable to reveal the greater SSC pulse.

The model-simulated distribution of the FM thickness along the navigation channel was also compared with the observed data (Fig. 9a). Since the measurements were made during the cruise survey on August 12, the comparison was made based on the 24-h averaged FM thickness on that day. The comparison showed that the FM model reasonably matched the major distribution pattern of the FM, particularly at sites from CS7 to CS10 in the low reach of the North Passage: the region of FM occurrence was well reproduced. The model-simulated FM thickness was about 1.6 m. Although, in this region, the model results had more peaks and troughs, it produced magnitudes similar to be observations. Considering that these measured data were an average of values measured on the cruise over a 2-3 km distance, the FM model robustly captured the dynamics of FM formation.

The FM model contains various prescribed parameters that are listed in Table. 2, such as sediment concentration within FM (C_m), the friction coefficients at two material interfaces (f_s and f_m) and dewatering efficiency (V_0). The modeling sensitivity for the FM layer could be assessed. The model was configured with different settings for these parameters. f_m, f_s and $V_0$are set to +10% larger and -10% smaller than the original configuration as shown in Table. 2. The C_m was specified as +5% larger and -5% smaller.

The sensitivity testing results is shown in Fig. 9b. It indicates that the FM model was not sensitive to $f_m$and f_s. With smaller changes, these two parameters demonstrated weak or moderate fluctuations, compared with original results. But dewatering velocity and mud concentration showed the significant sensitivity during the FM modeling. Particularly, smaller C_m and V_0 could produce much thicker FM layer. There is approximately a 20 cm increase on the thickness of the FM layer from CS7 to CS10 and outer region (Fig. 9b). The FM could be extended to CSW and CS3 region under these two conditions. The increase of C_m and V_0 could lead to smaller prediction for the thickness of FM layer.

5 Formation, transport and breakdown of FM

The tide current, waves, suspended sediment, saltwater intrusion, and mixing via stratification are major physical processes in the Changjiang River Estuary. These processes nonlinearly interacted each other to mutually lead to the formation, extension and breakdown of the FM. Using a two-layer FM model, we analyzed the relative contributions of individual processes, especially to the temporal and spatial variations of the FM.

5.1 Formation of FM

At selected sites in the middle of navigational channel from inner CSWM and CS7M to outer CS4M and CS10M, the time series of the simulated FM thickness clearly showed that the FM originally formed in the outlet region of the North Passage and then propagated landward into the upstream channel (Fig. 10). The FM first appeared at CS4M at the end of August 5, gradually increased in thickness starting from August 7, one day before the typhoon landed, and reached a peak thickness of ~120 cm on August 10 (Fig. 10c). A similar pattern was observed at site CS10M, with a few hours' time lag relative to CS4M (Fig. 10d). At this site, the maximum FM thickness was ~175 cm, occurring on August 10, nearly two days after the typhoon landed. At the inner site CS7M, the FM formed with a two-day delay (Fig. 10b), and its thickness was never as high as that at the outer CS4M and CS10M locations. At this site, the maximum FM thickness was less than 1.0 m. The model results also revealed that the FM thickness oscillated significantly at this site, suggesting that the FM was influenced by strong local source/sink effects and by lateral transport. The site CSWM, however, did not show any occurrence of the FM (Fig. 10a). This result was in good agreement with observations (Fig. 9a).

The time evolution of the FM also showed a remarkable tidal influence. Four typical snapshots, T1 to T4, were selected in this analysis, which covered the main period of the FM occurrence (Fig. 10). When the typhoon-induced strong wind swept the North Passage, H_s increased significantly after T1. The FM accumulation started on August 8, and the maximum H_s occurred as the typhoon reached its closest position to the North Passage (Fig. 10). T1 was the time at which a significant FM formed at CS4M within the North Passage, then CS10M was covered by the FM shortly at T2. The formation stage can be determined by the time duration from T1 to T2.

Snapshots at the formation stage (T1 to T2) of the FM were used to determine the spatial variability of the FM (Fig. 11). It was clear that the FM started to form around CS4M and CS10M in the outlet region of the North Passage at 18:00 August 7, with its thickness rapidly reaching ~65 cm in the initial stage before the typhoon landfall (Fig. 11a). The FM then significantly accumulated and covered the channel area from CS4M to CS10M at T2 (Fig. 11b). Snapshots of the SSC on an along-channel section overlapped with the FM and water movement velocities showed that at the initial stage of FM formation, the lower part of the water column, in the lower reach of the North Passage, was occupied by the high-concentration sediment suspension (Fig. 12a). The SSC concentration was mainly > 4 g/L, with a value of > 8 g/L near CS10M. As a result, a thick FM formed near CS10M at T1 (Fig. 11a and 12a). At this time, the tidal current flowed seaward and pushed the FM in the same direction. Near the bottom, however, the tidal current was only ~0.1-0.2 m/s, so that its influence on the FM movement was weak. This explains why the velocity of the FM layer was only ~0.05 m/s, and the whole FM layer was relatively thin.

At T2, when the typhoon-induced maximum wind occurred, the strongest surface waves created much greater SSCs in the suspension layer in the lower reach of the North Passage (Fig. 12b). The mixing was significantly enhanced by wave-current interactions. As a result , the high-SSC water not only dominated the bottom, but also entrained into the middle of the water column. The FM then flowed upstream following the ambient tidal flow. Under these conditions, the FM flow velocity was ~0.2 m/s near CS4M.

In this study, the stratification was estimated based on the salinity front in the water column. Along the channel section, the vertical distribution of FM and corresponding salinity indicated that there was a strong saltwater intrusion into the North Passage (Fig. 13). In the early and growing stages of the FM during the moderate tide, the salinity front was not very strong. The vertical salinity gradient was also not very large, suggesting tidal mixing was still significant in this period (Fig. 13a). At T2, under a similar tidal condition, the water remained vertically well-mixed (Fig. 13b).

The typhoon caused strong impacts on various dynamics mentioned above, including wave, flow and stratification. To determine the triggering physical processes leading to the FM formation, three additional numerical experiments were made. The first experiment considered the effect of typhoon waves on the flow, sediment and FM. In this experiment, the typhoon wave forcing was not included in the hydrodynamic modeling. We called it to be the no-wind case. The second experiment considered the effect of typhoon winds on hydrodynamics, but the wave impact was not included. We call it to be the no-wave case. The third experiment considered the effect of both typhoon-induced winds and waves on the flow, suspended sediment and FM. In this experiment, no stratification was taken into account, so we called it to be the barotropic case. In all the three cases, the water column sediment and FM models followed the configuration as shown in Table 2 without any modifications.

Taking the formation process at CS4M as an example, the results of these three experiments are shown in Fig. 14, and they were compared with the result from original simulation shown in Fig. 10c. We found that the wave was not an essential factor for the FM formation. Without the wave impact, the FM could still form and grow thicker. The thickness of the FM was about 10 cm higher compared with the original simulation result. In this case, the near-bottom shear stress was smaller, suggesting a weaker turbulent energy on the FM-suspension interface. It led to a weaker entrainment and thus a thicker FM layer.

The results from the no-wind and barotropic cases suggested that the stratification was the key physical process leading to the FM formation. The no-wind condition was still able to produce the significant formation of the FM, with the magnitude of ~40-70 cm. In this case, the FM occurred with about 3-day delay. This result implied that the FM could be formed even without the typhoon-wind impact. The barotropic case, however, showed no FM generation, no matter whether typhoon-induced waves and winds activated or not. The only difference between the no-wind and barotropic cases was the level of stratification. Therefore, it was no doubt that the stratification is a necessary condition that is a triggering effect for the FM formation.

The no-wind and original experiments suggested that the typhoon wind did have a significant influence on the massive formation of the FM. The strong surface wind significantly modified the flow condition and stratification. Under the no-wind condition, the distributions of the flow and salinity along the channel showed that the saltwater intrusion was much weaker than that in the original simulation. The isohalines in the no-wind scenario had greater extension at selected four snapshots. At T1, the isohalines of 5.0 to 15 PSU at the intrusion front covered an about 15-km length of the channel (Fig. 15a). Whereas in original simulation, the along-chancel length covered by these isohalines was less than 10 km. In the vertical, the salinity gradient at CS10M was much stronger in the original case than in the no-wind case. For the other three selected times, the salinity gradients around the intrusion front were much stronger under the condition with a full typhoon impact (Fig. 13b-d) than that in the no-wind scenario (Fig. 15b-d). The thickness and FM coverage were both smaller than that in the case with the typhoon. In fact, the typhoon wind strongly enhanced the saltwater intrusion and thus intensified the degree of stratification. Therefore, stratification was the key physical process producing the massive formation of FM.

Previous observational and modeling studies have confirmed that stratification via vertical mixing have strong effects on the FM dynamics (Geyer et al., 1993; Winterwerp, et al., 1999; Ge et al., 2018). Additionally, in an estuary, the lateral and vertical mixing between the low-salinity fresher water and high-salinity sea water can create the complicated haloclines, and establish a baroclinic pressure gradient force. The salinity-induced density gradient, in turn suppresses the production of turbulent kinetic energy in the water column and hence weakens vertical mixing (Geyer et al., 2011), which can greatly modulate suspended sediment advection and diffusion (Liu et al., 2011; Ren and Wu, 2014; Ge et al., 2018).

5.2 Transport of FM

After the FM began to form, the astronomical tides transitioned from the spring phase (T2) to neap phase (T3). This period was defined as an extension stage of the FM. During the time from

T2 to T3, the near-bottom currents reached ~1.5 m/s at all four sites, suggesting strong tidal mixing in that region, followed by thickness oscillations at CS10M, CS4M, and CS7M (Fig. 10). It expanded seaward along the channel, and also gradually propagated upstream, with the FM center shifting to the channel near CS4M, and finally reaching CS7M (Fig. 11c). The maximum thickness was above 1.5 m at CS4M, dropped to 70 cm at CS10M, and was 83 cm at CS7M. By T3, however, the FM appeared as isolated patches in the northern shoal, with a thickness of 15~50 cm. This explains why a high SSC was observed at the shoal sites during the field campaign (Table 1), suggesting that the FM could have formed and been transported into the shallow shoals.

At T3, the FM thickness reached its maximum. At this time, the SSC significantly decreased, but the high-SSC bottom water was still visible in the suspension layer (Fig. 12c). A relatively stronger flow was found in the lower column around CS7M, with a velocity of about 1.0 m/s near the bottom and of almost zero near the surface. This caused the FM to flow at a higher speed. The velocity reached 0.4 m/s and 0.1 m/s at the onshore-extension FM head and tail, respectively.

During the neap tide, the saltwater intrusion extended upstream into the middle area of the channel. At T3, the FM thickness reached its maximum value and the salinity front reached the area near CS2M (Fig. 13c). The near-bottom layer around the middle area near CSWM was dominated by high-salinity water (Fig. 13d).

It was found that the FM locations were highly correlated with the salinity haloclines in the saltwater intrusion front. FM extension mainly followed this front (Fig. 13). It can be inferred that salinity-induced stratification was a major factor in the maintenance of high SSC in the suspension layer and in FM formation. This relationship was suggested by previous studies in the Changjiang Estuary (Ge et al., 2018; Wan and Wang, 2018; Li et al., 2018), similar dynamic regions in the Magdalena River of Colombia (Restrepo et al., 2018) and in the Rhine-Meuse estuary (De Nijs and Pietrzak, 2011).

Stratification could also be enhanced by sediment distribution (Geyer, 1993; Winterwerp, 2001, 2006; Ge et al., 2018). The high SSC in the suspension layer corresponded with the intrusion front, and strongly influenced the near-bottom part of the water column (Fig. 12). With high SSC above the FM (Table 1), the sediment-induced vertical density gradient was strong; intensifying the stratification. The combined effect of salinity and sediment weakened vertical mixing that produced the extension of FM at the intrusion front. Therefore, under the extension stage, the transport of FM was consequently controlled by the saltwater intrusion. The extension edge of FM was constrained within the salinity front.

5.3 Breakdown of FM

On August 8-9, after the typhoon passed, the tide transitioned to the neap phase from T3 to T4. At these three sites, the FM thicknesses all reached their maximum values within the neap tide. Over this period, after the typhoon passed, H_s dropped substantially and the currents reached a minimum of 1.0 m/s at all three sites.

At T4, the SSC in the suspension layer significantly decreased. Under the weak tidal and wave conditions in the neap tide, SSC in the channel was low (Fig. 12d). FM movement still followed the ambient tidal currents and saltwater intrusion (Fig. 13d). The head of the FM body continued a rapidly landward movement, to arrive at a location near CSWM, and a seaward movement to arrive at a location near to CS10M. As a result, the FM was more evenly distributed along the channel.

Although the FM reached its maximum during the neap tide, it showed a decreasing trend over the period from T3 to T4. Therefore, it experienced the breakdown stage after T4. After the neap tide period, the tidal current gradually increased. On August 15, the magnitude of the tidal velocity was 1.5 m/s during the neap-spring transition, and then on August 17-18, it was up to ~ 3.0 m/s during the spring tide. During this period, H_s was low, about 0.5 m in the outlet area and 0.25 m at CSWM (Fig. 10). Under these physical conditions, FM continued to diminish. It almost disappeared on August 17. After that, the weakened FM was only visible at CS4M and CS10M, with a thickness of < 50 cm. This was consistent with the SSC measurements, which showed an extremely high SSC of 87.6 g/L during the spring tide (Table 1).

Under FM breakdown stage, the patches over the shoal decreased remarkably (Fig. 11d), although the FM still continued to propagate near CSWM at 20:00 August 12. The channel of the lower reach of the North Passage was then covered by the FM, with a thickness in the range of 0.3 m to 1.35 m (Fig. 11d). Most of the FM was then limited to the navigation channel.

6 Discussions

6.1 Contributions of source and sink terms

The formation and breakdown of the FM were mainly determined by the source and sink terms in Eq. 13, including $Settling$, $Entrainment$, $Erosion$, and $Dewatering$. The spatial distributions of these terms and their sum at T2, as an example, are shown in Fig. 16. The results show an active sediment exchange between the two interfaces in the North Passage. The FM existed only in a narrow channel from CS4M to CS10M, whereas no FM was detected in the other regions. The sediment settling had a spatially smoothed distribution around the no-FM region (Fig. 16a). The SSC was mainly controlled by conventional sediment dynamics; only settling and erosion occurred in this region. Without the FM, the $Entrainment$ equaled the $Erosion$ (Fig. 16b and 16d). This situation applied to most of the North Passage. At T2, the water velocity was relatively strong in the channel between CSWM and CS4M (Fig. 10). The bottom shear stress produced strong sediment erosion around CSWM and near main channel (Fig. 16d). A difference between the entrainment and bed erosion only occurred around the FM-covered region, mainly in the channel around CS4M (Fig. 16b). There was a significant entrainment process, which was especially large around the landward tip of the FM near CS4M. At this time, the FM flow at CS4M was weak, and the upper ambient flow was relatively strong (Fig. 13b). According to Eq. 15, the entrainment was highly related to the magnitude of $u - u_m$. The large velocity difference between the suspension layer and the FM suggested strong turbulent mixing and active mass exchange at the interface, which led to a relatively strong entrainment around the landward tip. On the other hand, the FM flow was slow, which was insufficient to produce bed erosion in the FM-covered channel (Fig. 16d). Dewatering only occurred beneath the FM (Fig. 16c). The sum of these four terms showed a similar distribution pattern (Fig. 16e). The upper reach of the North Passage was dominated by sink effects, suggesting that the sediment was mainly eroded into the suspension layer, which was unfavorable to the FM formation (Fig. 16e). The lower reach was mainly controlled by source effect, suggesting that the sediment settling dominated. The shallow shoals within the groynes also had a significant positive net contribution to the FM (Fig. 16e). These shallow shoals can apparently also accumulate sediment, making them a potential place for the FM formation.

During the breakdown stage, T4, the source and sink terms had quite different distributions than that in the growth stage (Fig. 17). Sediment settling became weak compared with the conditions at T2 (Fig. 17a). In the velocity-decreasing phase during the neap tide, the tidal flow was weak at T4, which led to weak erosion and entrainment. The entrainment was also weak above the FM-covered area, except at the landward tip between CSWM and CS7M (Fig. 17b). It had similar dynamics to those at T2, with a larger FM flow velocity at the extension edge and weaker ambient flow (Fig. 13d). It produced a significant amplitude of $u - u_m$, leading to entrainment. Dewatering was uniform through the FM coverage. According to Eq. 17, the dewatering process was only related to the consolidation rate and FM concentration. In this study since these two attributes were spatially uniform and temporally constant parameters, they inevitably produced uniform dewatering at the FM-bed interface. The sum of four source/sink terms demonstrated that the net effect was negative at T4 (Fig. 17e). It suggested that the dewatering and entrainment dominated the breakdown process of the FM. In the following spring tide, the entrainment contribution strongly grew as a result of energetic tide currents and enhanced mixing. With the joint effect of dewatering and tide-induced entrainment, the FM eventually experienced a strong breakdown process in the spring tide.

6.2 Contribution of bed property on the mud source

Ultimately, bed-stored sediment was the major mud source for the FM. The distribution and variation of this source was controlled by external driving forces, such as tidal mixing and wave-current interaction-produced bottom shear stress. The sediment properties in the seabed influence the sediment amount eroded to the water column, which functioned as a final material source into the FM in following rapid sediment settling. Fine grain-size sediment was the major component in the FM (Winterwerp, 1999). Therefore, the occurrence of the FM was dynamically related to sea bed sediment size and classification.

The North Passage is dominated by the fine sediment with grain size smaller than 20 μm (Fig. 4a), suggesting an abundant mud source for the FM formation. The lower reach of North Passage had clay content > 20%, even > 30% around seaward outlet near CS4M and CS10M (Fig. 4b). This outlet region provided adequate clay materials for the FM formation, as well as the upper suspension. Energetic conditions produced strong sediment erosion into the water column. With moderate and weak vertical mixing during the transition to the neap tide, the sediment suspension accumulated in the near-bottom layer and formed the FM. Since the bed provided a necessary material availability for the sediment source of the fluid mud layer, the bed sediment property was an essential factor during the formation stage of the FM.

6.3 Local dredging impact

Significant FM formation between CS9 and CS2 (Fig. 3) was observed. However, the numerical model failed to reproduce this (Fig. 9a). The FM thickness at that area was about 75 cm and its formation did not follow the mechanism discussed above. The FM was only detected in a narrow region. The model did not capture any local formation or lateral transport of FM into this region. This difference was probably related to anthropogenic effects in the local channel . To maintain an adequate cargo-shipping depth, dredging is undergoing along the navigational channel as a daily routine activity (Pan et al., 2012; Dai et al., 2013; Wang et al., 2015). Some particular locations within the groyne area are selected as a temporary storage for dredged mud. One groyne region between N3 and N4 happened to be a storage site. These sediments would eventually be pumped onto the nearby Hengsha Shoal for land reclamation (Liu et al., 2011). Part of this stored mud had the chance to return to the main channel. During the typhoon passage, the surface waves were not high in the main channel. According to the modeling results, H_s around the CS was about 0.5 m. It was not sufficient to produce a high bottom shear stress, but it was adequate for significant wave-induced stress and disturbance on the shallow shoal between N3 and N4. Previous tripod measurement found a notable cross-channel, southward flow (Ge et al., 2018), which potentially carried the mud from the shallow shoal within the groynes to the deep channel. This flow pattern and the storage of dredging within the shoal could play an important role in the FM formation around CS2.

7 Conclusion

A comprehensive field campaign in the area of maximum turbidity in the North Passage of the Changjiang Estuary detected the FM formation after a severe typhoon. The observations showed a greater FM development on spatial and vertical spaces during the neap tide. The SSC was generally above 50 g/L, with a maximum of 87.8 g/L. The FM was predominantly in the near-bottom layer within the navigational channel. The spatial and temporal variability of the FM co-occurred with a strong saltwater intrusion, which led to the pronounced stratification in the neap tide. Acoustic measurements revealed that the FM occurred mainly in the lower reach of the North Passage, with a maximum thickness of ~0.9 m.

A two-layer modeling approach, with an upper suspension layer and a lower FM layer, simulated the formation, transport and breakdown of the FM over a period during Typhoon Haikui. This approach was based on the unstructured-grid FVCOM model with the inclusion of full wave-current interactions. The model successfully revealed that the typhoon strongly intensified the stratification level in the outlet region, which essentially led to the FM formation. The simulation indicated that the FM formed under increased stratification about one day before the typhoon landed, and reached its maximum two days after the typhoon passed. Subsequent weak mixing in the neap tide sustained the FM. In the subsequent period of moderate and spring tides, when mixing in the upper water column became stronger, the FM entered its breakdown stage. The simulation results also showed that the FM experienced a strong propagation process. It formed mainly in the outlet region, and gradually extended landward along the channel under the influence of the saltwater intrusion. Eventually, it occupied nearby shallow shoal areas outside the North Passage. The landward extension boundary of the FM had active entrainment as a result of larger velocity difference between FM and ambient tidal flow.

Acknowledgments

J. Ge, P. Ding, K. Ke and J. Yi are supported by the National Key R&D Program of China (Grant No. 2016YFA0600903) and the NSFC project (Grant No. 41776104). Z. Wang is supported by the KNAW project (Grant No. PSA-SA-E-02). C. Chen is supported by his Montgomery Charter Chair fund for his time and also the travel fund from the International Center for Marine Studies (ICMS) at Shanghai Ocean University (SHOU).The two-layer model used in this study has been included in the latest FVCOM version 5.0, which will be freely available (http://code.fvcom.org/medm). All datasets used in this work is publicly available at https://figshare.com/s/6c5b19b2f9dab52f87fe. Authors would like to thank two anonymous reviewers and Editor Chris Sherwood for providing constructive comments and suggestions on the manuscript.

References

Chen, J., Li, D., Chen, B., Hu, F., Zhu, H., & Liu, C. (1999). The processes of dynamic sedimentation in the Changjiang Estuary. *Journal of Sea Research*, 41(1-2), 129–140.

Chen, C., Liu, H., Beardsley, R.C., (2003). An unstructured, finite-volume, three- dimensional, primitive equation ocean model: application to coastal ocean and estuaries. *Journal of Atmospheric and Oceanic Technology* 20, 159–186.

Chen, C., Beardsley, R.C., Cowles, G., 2006. An unstructured grid, finite-volume coastal ocean model (FVCOM) system, Special Issue entitled ‘‘Advance in Computational Oceanography’’. *Oceanography* 19 (1), 78–89.

Chen, C., P. Xue, P. Ding, R. C. Beardsley, Q. Xu, X. Mao, G. Gao, J. Qi, C. Li, H. Lin, G. Cowles, M. Shi, (2008). Physical mechanism for the offshore detachment of the Changjiang diluted water in the East China Sea, *Journal of Geophysical Research*, 113, C02002, doi. 10.1029/2006JC003994.

Chen, C., Beardsley, R., Cowles, G. et al. (2013), An unstructured grid, finite-volume community ocean model FVCOM user manual, SMAST/UMASSD-13-0701, New Bedford, Mass. [Available at http://fvcom.smast.umassd.edu/fvcom/.]

Corbett DR, Dail M, Mckee B (2007) High-frequency time-series of the dynamic sedimentation processes on the western shelf of the Mississippi River Delta. *Cont Shelf Res* 27(10–11): 1600–1615

Dai, Z., Liu, J. T., Fu, G., & Xie, H. (2013). A thirteen-year record of bathymetric changes in the North Passage, Changjiang (Yangtze) estuary. *Geomorphology*, 187(C), 101–107. http://doi.org/10.1016/j.geomorph.2013.01.004

De Nijs, M. A. J., & Pietrzak, J. D. (2011). An explanation for salinity-and SPM-induced vertical countergradient buoyancy fluxes. *Ocean Dynamics*, 61(4), 497–524.

Eidam, E. F., Ogston, A. S., & Nittrouer, C. A. (2019). Formation and Removal of a Coastal Flood Deposit. Journal of Geophysical Research-Oceans, 124(2), 1045–1062. http://doi.org/10.1029/2018JC014360

Ge, J., Chen, C., Qi, J., Ding, P., & Beardsley, R. C. (2012). A dike–groyne algorithm in a terrain-following coordinate ocean model (FVCOM): Development, validation and application. *Ocean Modelling*, 47(C), 26–40. http://doi.org/10.1016/j.ocemod.2012.01.006

Ge, J., Ding, P., Chen, C., Hu, S., Fu, G., & Wu, L. (2013). An integrated East China Sea–Changjiang Estuary model system with aim at resolving multi-scale regional–shelf–estuarine dynamics. *Ocean Dynamics*, 63(8), 881–900. http://doi.org/10.1007/s10236-013-0631-3

Ge, J., Shen, F., Guo, W., Chen, C., & Ding, P. (2015). Estimation of critical shear stress for erosion in the Changjiang Estuary: A synergy research of observation, GOCI sensing and modeling. *Journal of Geophysical Research-Oceans*, 120(1), 8439–8465. http://doi.org/10.1002/2015JC010992

Ge, J., Zhou, Z., Yang, W., Ding, P., Chen, C., Wang, Z. B., & Gu, J. (2018). Formation of Concentrated Benthic Suspension in a Time-Dependent Salt Wedge Estuary. *Journal of*

Geophysical Research-Oceans, 123(11), 8581–8607. http://doi.org/10.1029/2018JC013876

Geyer, W. R. (1993). The importance of suppression of turbulence by stratification on the estuarine turbidity maximum. *Estuaries*, 16(1), 113–125. http://doi.org/10.2307/1352769

Guan, W. B., Kot, S. C., & Wolanski, E. (2005). 3-D fluid-mud dynamics in the Jiaojiang Estuary, China. *Estuarine, Coastal and Shelf Science*, 65(4), 747–762. http://doi.org/10.1016/j.ecss.2005.05.017

Hale, R. P., Ogston, A. S., Walsh, J. P., & Orpin, A. R. (2014). Sediment transport and event deposition on the Waipaoa River Shelf, New Zealand. Continental Shelf Research, 86(C), 52–65. http://doi.org/10.1016/j.csr.2014.01.009

Hsu, T.-J., Ozdemir, C. E., & Traykovski, P. A. (2009). High-resolution numerical modeling of wave-supported gravity-driven mudflows. Journal of Geophysical Research, 114(C5), F04016–15. http://doi.org/10.1029/2008JC005006

Knoch D. and Malcherec A (2011) A numerical model for simulation of fluid mud with different rheological behaviors. *Ocean Dyn* 61(2): 245–256

Le Hir, P., Bassoullet, P., & Jestin, H. (2000). Application of the continuous modeling concept to simulate high-concentration suspended sediment in a macrotidal estuary. In Proceedings in Marine Science (Vol. 3, pp. 229–247). Elsevier. http://doi.org/10.1016/S1568-2692(00)80124-2

Li, L., He, Z., Xia, Y., & Dou, X. (2018). Dynamics of sediment transport and stratification in Changjiang River Estuary, China. *Estuarine, Coastal and Shelf Science*, 213, 1–17. http://doi.org/10.1016/j.ecss.2018.08.002

Liu, G., Zhu, J., Wang, Y., Wu, H., & Wu, J. (2011). Tripod measured residual currents and sediment flux: Impacts on the silting of the Deepwater Navigation Channel in the Changjiang Estuary. *Estuarine, Coastal and Shelf Science*, 93(3), 192–201. http://doi.org/10.1016/j.ecss.2010.08.008

Ogston, A. S., Cacchione, D. A., Sternberg, R. W., & Kineke, G. C. (2000). Observations of storm and river flood-driven sediment transport on the northern California continental shelf. Continental Shelf Research, 20(16), 2141–2162. http://doi.org/10.1016/S0278-4343(00)00065-0

Pan, L., Ding, P., & Ge, J. (2012). Impacts of Deep Waterway Project on Morphological Changes within the North Passage of the Changjiang Estuary, China. *Journal of Coastal Research*, 284, 1165–1176. http://doi.org/10.2112/JCOASTRES-D-11-00129.1

Pu, X., Shi, J. Z., Hu, G.-D., & Xiong, L.-B. (2015). Circulation and mixing along the North Passage in the Changjiang River estuary, China. *Journal of Marine Systems*, 148(C), 213–235. http://doi.org/10.1016/j.jmarsys.2015.03.009

Ren, J. and Wu, J. (2014). Sediment trapping by haloclines of a river plume in the Pearl River Estuary. *Continental Shelf Research*, 82(c), 1–8. http://doi.org/10.1016/j.csr.2014.03.016

Restrepo, J. C., Schrottke, K., Traini, C., Bartholomae, A., Ospino, S., Ortíz, J. C., et al. (2018). Estuarine and sediment dynamics in a microtidal tropical estuary of high fluvial discharge: Magdalena River (Colombia, South America). *Marine Geology*, 398, 86–98. http://doi.org/10.1016/j.margeo.2017.12.008

Traykovski, P., Geyer, W. R., Irish, J. D., & Lynch, J. F. (2000). The role of wave-induced density-driven fluid mud flows for cross-shelf transport on the Eel River continental shelf. Continental Shelf Research, 20(16), 2113–2140. http://doi.org/10.1016/S0278-4343(00)00071-6

Traykovski, P., Trowbridge, J., & Kineke, G. (2015). Mechanisms of surface wave energy dissipation over a high-concentration sediment suspension. Journal of Geophysical Research-Oceans, 120(3), 1638–1681. http://doi.org/10.1002/2014JC010245

Wan, Y., Roelvink, D., Li, W., Qi, D., & Gu, F. (2014). Observation and modeling of the storm-induced fluid mud dynamics in a muddy-estuarine navigational channel. *Geomorphology*, 217, 23–36. http://doi.org/10.1016/j.geomorph.2014.03.050

Wan, Y., & Wang, L. (2017). Numerical investigation of the factors influencing the vertical profiles of current, salinity, and SSC within a turbidity maximum zone. *International Journal of Sediment Research*, 32(1), 20–33. http://doi.org/10.1016/j.ijsrc.2016.07.003

Wang, Z. B. and J. C. Winterwerp, 1992. A model to simulate the transport of fluid mud. Tech. Rep. Z163, WL | Delft Hydraulics, Delft, The Netherlands.

Wang, Z. B., van Maren, D. S., Ding, P. X., Yang, S. L., Van Prooijen, B. C., De Vet, P. L. M., et al. (2015). Human impacts on morphodynamic thresholds in estuarine systems. *Continental Shelf Research*, 1–10. http://doi.org/10.1016/j.csr.2015.08.009

Wang L, Winter C, Schrottke K, Hebbeln D, Bartholoma A (2008) Modelling of estuarine fluid mud evolution in troughs of large subaqueous dune. Proceedings of the Chinese-German joint symposium on hydraulic and ocean engineering. Eigenverlag, Darmstadt, 372–379

Warner, J. C., Sherwood, C. R., Signell, R. P., Harris, C. K., & Arango, H. G. (2008). Development of a three-dimensional, regional, coupled wave, current, and sediment-transport model. *Computers and Geosciences*, 34(10), 1284–1306. http://doi.org/10.1016/j.cageo.2008.02.012

Winterwerp, J. (1999). On the dynamics of high-concentrated mud suspensions. Ph.D. thesis, Delft University of Technology

Winterwerp, J. (2002). Scaling parameters for High-Concentrated Mud Suspensions in tidal flow. Proceedings in Marine Science, 5, 171–186.

Winterwerp, J. C., Wang, Z. B., Kester, J. A. T. M. V., & Verweij, J. F. (2002). Far-field impact of water injection dredging in the Crouch River. *Maritime Engineering*, 154(4), 285–296. http://doi.org/10.1680/maen.154.4.285.38905

Winterwerp, J. and W. Van Kesteren, (2004). Introduction to the physics of cohesive sediment in the marine environment, Developments in sedimentology 56. Series editor: T. Van Loon

Winterwerp, J. (2006). Stratification effects by fine suspended sediment at low, medium, and very high concentrations. *Journal of Geophysical Research*, 111, C05012.

Winterwerp, J. C. (2011). Fine sediment transport by tidal asymmetry in the high-concentrated Ems River: indications for a regime shift in response to channel deepening. *Ocean Dynamics*, 61(2), 203–215.

Wu, J., Liu, J. T., & Wang, X. (2012). Sediment trapping of turbidity maxima in the Changjiang Estuary. *Marine Geology*, 303-306(C), 14–25. http://doi.org/10.1016/j.margeo.2012.02.011

Xue, P., C. Chen, P. Ding, R. C. Beardsley, H. Lin, J. Ge, and Y. Kong, (2009). Saltwater intrusion into the Changjiang River: A model-guided mechanism study, *Journal of Geophysical Research*, 114, C02006, doi:10.1029/2008JC004831.

Xie M, Zhang W, Guo W (2010) A validation concept for cohesive sediment transport model and application on Lianyungang Harbor, China. *Coast Eng* 57(6):585–596

Yang, S. L., Milliman, J. D., Li, P., & Xu, K. (2011). 50,000 dams later: Erosion of the Yangtze River and its delta. *Global and Planetary Change*, 75(1), 14–20. http://doi.org/10.1016/j.gloplacha.2010.09.006

Yang, X., Zhang, Q., & Hao, L. (2015). Numerical investigation of fluid mud motion using a three-dimensional hydrodynamic and two-dimensional fluid mud coupling model. *Ocean Dynamics*, 65(3), 449–461. http://doi.org/10.1007/s10236-015-0815-0

Tables and Captions

Table 1. Sediment concentrations at measurement sites. The labels "S" and "N" in the timing column indicate the maximum SSC in bottom layer occurred in the spring and neap cycle, respectively.

Survey site	SSC range in the upper five layers (g/L)	Maximum SSC in the bottom layer (g/L)	Timing of SSC maximum
CS9S	0.013-0.853	1.46	S
CS9M	0.023-1.130	2.18	S
CS2S	0.024-1.720	7.41	N
CS2M	0.048-4.860	87.80	N
CS6N	0.021-3.110	12.80	S
CS6M	0.047-4.440	69.90	N
CS6S	0.016-4.670	21.80	S
CSWN	0.005-4.470	26.40	N
CSWM	0.039-8.340	48.60	N
CSWS	0.029-7.930	40.70	S
CS3N	0.005-5.250	17.70	N
CS3M	0.013-5.690	77.30	S
CS3S	0.012-5.510	12.30	S
CS7M	0.030-4.780	9.53	S
CS7S	0.005-9.820	14.20	S
CS4M	0.004-6.920	74.50	N
CS4S	0.002-3.950	8.28	S
CS0S	0.005-0.953	1.26	S
CS0M	0.000-0.216	0.23	N
CS10S	0.003-2.650	2.21	S
CS10M	0.002-1.760	87.60	S

Table 2. Parameters for the nesting models.

	Model for estuary	Model for North Passage
cells	93848	23351
nodes	49854	12079
Time step for external mode	1.0	0.5
mode split ratio	10	5
vertical layers	20	
horizontal mixing coefficient	0.1	
vertical mixing coefficient	1.0×10^{-4}	
τ_{dm}	0.1 N/m^2	
C_m	200 g/L	
M_e	2.0×10^{-4} $kg/(m^2s)$	
C_s	0.25	
C_σ	0.42	
f_s	0.032	
f_m	0.05	
τ_{ce}	0.2-1.8 N/m^2	
ω_s	0.6 mm/s	
ρ_m	1.1×10^3 g/L	
ρ_s	1.0×10^3 g/L	
V_0	4.0×10^{-6} m/s	
$R_{\Delta t}$	10	

Figure 1. (a): Bathymetry of the Changjiang Estuary and adjacent coastal region, inserted with a panel for the track of Typhoon Haikui originated from Iwo Jima during August, 2012. (b): An enlarged view of the North Passage with dikes and groynes along the nearby Hengsha Shoal and Jiuduansha Shoal. Dashed red lines represent the navigation channel. The blue dots in two panels indicate the buoy locations for wind and wave observations. The black dots indicate the sampling sites for bed sediment. The red dots indicate mooring survey sites for hydrodynamics and suspended sediment, which were arranged along cross-channel sections. They are labeled with suffixes *N*, *M* or *S*, indicating locations in the north, middle, and south of the navigation channel.

Figure 3. The measured depth from low-, and high-frequency sonars along the navigation channel (a). The thickness and accumulated FM determined from the depth differences between the sonars (b).

Figure 4. Spatial distributions of median grain size d_{50} (a) and percentage of clay content ξ^{cl} (b) of the bed soil sediment. The black dots indicate the soil sampling sites.

Figure 5. Sketch of physical processes involved in FM dynamics, modified from Winterwerp (1999). The shade indicates the stratification in the water column.

Figure 6. The two grids used in the nested modeling. The overall model grid for the Changjiang Estuary and its adjacent coastal regions (a), its enlarged view around the North Passage (b) and the higher-resolution inner model grid within the North Passage (c). The blue curves indicate the nesting boundary between outer and inner domains.

Figure 7. The model-data comparisons for wind speed at 10-m height (left column) and significant wave height (right column) at buoys CJK (upper row), NPJ (middle row), and NCD (lower row). The blue stars and red curves indicate observed and modeled results, respectively.

Figure 8. Model-data comparisons between simulated (red curves) and directly sampled (black dots) suspended sediment concentrations in surface, middle and bottom layers at sites CS3S (a-c), CSWN (d-f), CS7S (g-i), and NGN4S (j-l).

Figure 9. (a): Model-data comparisons of thickness of the FM along the navigation channel. (b): Model sensitivity results for various parameters configurations, including $V_0(1 \pm 10\%)$, $f_s(1 \pm 10\%)$, $f_m(1 \pm 10\%)$ and $C_m(1 \pm 5\%)$. The data thickness uses the one-day averaged measurements from August 12, 2012.

Figure 10. The timeseries of simulated thickness of the FM (red curves), significant wave height (black curves) and tide current velocity (blue curves) from August 5 to 20 at selected middle-channel sites CSWM (a), CS7M (b), CS4M (c), and CS10M (d). T1, T2, T3, and T4 are four selected timings at 2012-08-07 18:00:00; 2012-08-08 08:00:00; 2012-08-10 14:00:00, and 2012-08-12 20:00:00, respectively.

Figure 11. Spatial distribution of the FM thickness within the North Passage at T1 (a), T2 (b), T3 (c), and T4 (d). Black dots indicate selected survey sites.

Figure 12. Vertical distributions of currents and SSC along the navigation channel at T1 (a), T2 (b), T3 (c), and T4 (d). The dark shades indicate the corresponding distribution of FM thickness along the channel. The blue and red arrows indicate the tidal current and FM flow, respectively. The arrow length and head size are scaled to current velocity.

Figure 13. Same as Figure 12, except that the colors indicate salinity.

Figure 14. The timeseries of simulated thickness of the FM from the original (red curve), no-wind (black curve), no-wave (green curve) and barotropic (blue curve) cases.

Figure 15. Same as Figure 13, except that modeled results are from the no-wind case.

Figure 16. Spatial distributions of deposition (a), entrainment (b), dewatering (c), erosion (d) occurring at the FM-bed and FM-suspension interfaces at the time T2. The sum of these four source/sink terms is also included (e). The black solid curves outline the coverage of FM.

Figure 17. Same as Figure 16, except at time T4.

Figure 1.

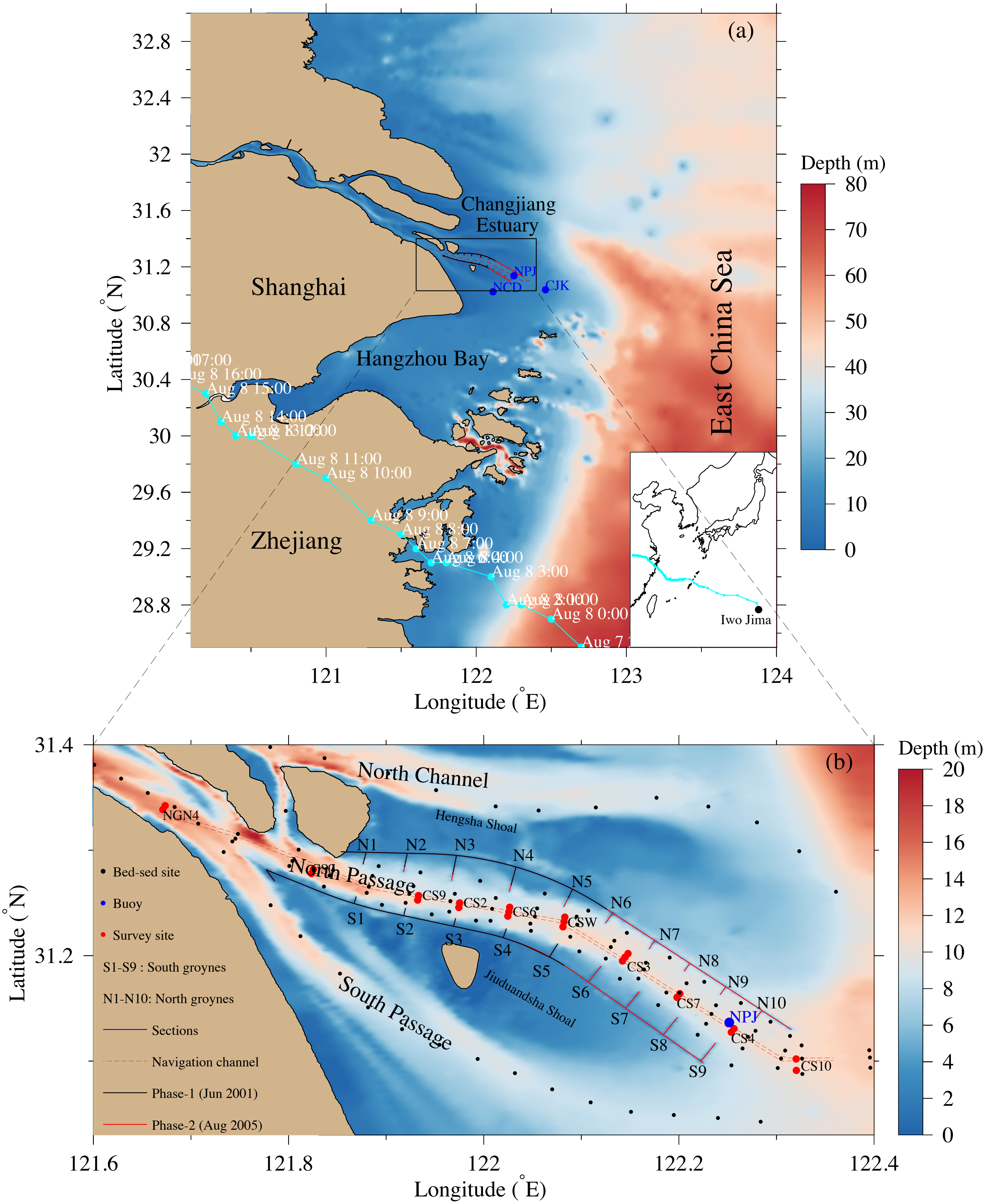

(a)
Latitude (°N)
Longitude (°E)
Shanghai
Zhejiang
Changjiang
Estuary
Hangzhou Bay
East China Sea
NPJ
NCD
CJK
Depth (m)
Iwo Jima
Aug 8 16:00
Aug 8 15:00
Aug 8 14:00
Aug 8 11:00
Aug 8 10:00
Aug 8 9:00
Aug 8 7:00
Aug 8 3:00
Aug 8 0:00
(b)
North Channel
Hengsha Shoal
North Passage
South Passage
Jiuduandsha Shoal
Bed-sed site
Buoy
Survey site
S1-S9 : South groynes
N1-N10: North groynes
Sections
Navigation channel
Phase-1 (Jun 2001)
Phase-2 (Aug 2005)
NGN4
CS9
CS2
CS6
CSW
CS3
CS7
CS4
CS10
NPJ
N1
N2
N3
N4
N5
N6
N7
N8
N9
N10
S1
S2
S3
S4
S5
S6
S7
S8
S9
Depth (m)
Latitude (°N)
Longitude (°E)

Fig.1

Figure 2.

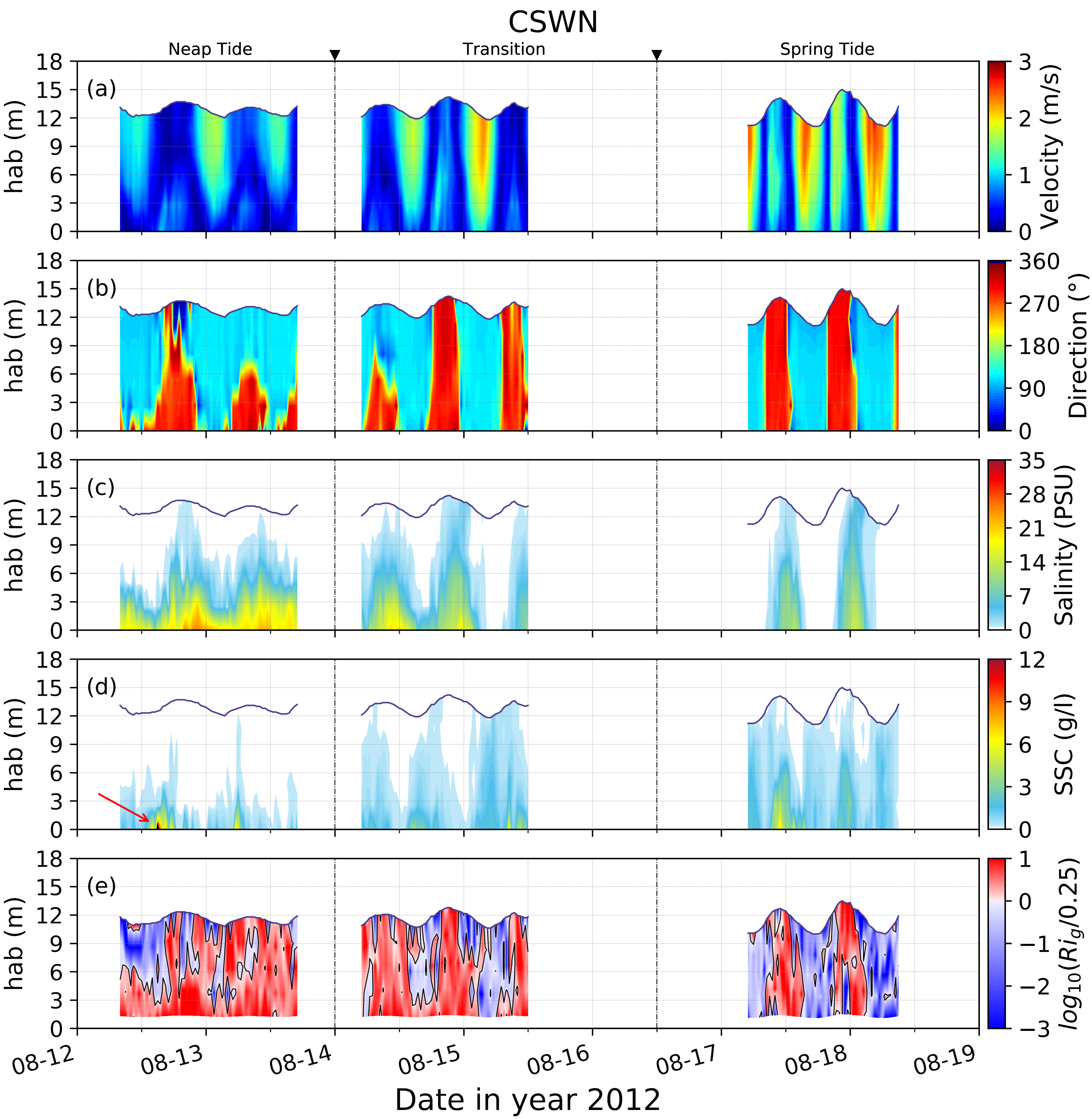
CSWN
Neap Tide
Transition
Spring Tide
(a)
(b)
(c)
(d)
(e)
hab (m)
Velocity (m/s)
Direction (°)
Salinity (PSU)
SSC (g/l)
$log_{10}(Ri_g/0.25)$
08-12
08-13
08-14
08-15
08-16
08-17
08-18
08-19
Date in year 2012

Fig. 2

Figure 3.

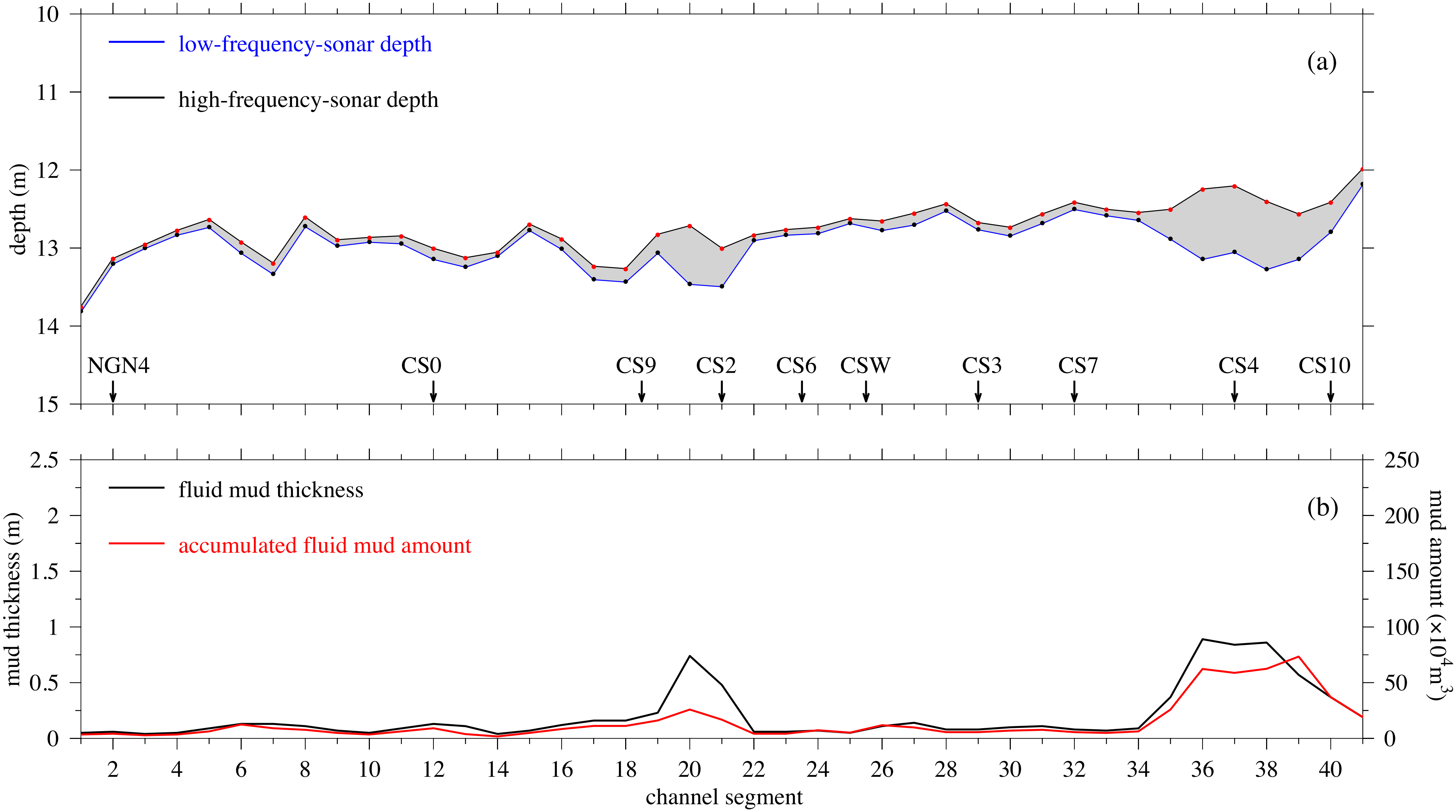

(a)
low-frequency-sonar depth
high-frequency-sonar depth
depth (m)
10
11
12
13
14
15
NGN4
CS0
CS9
CS2
CS6
CSW
CS3
CS7
CS4
CS10
(b)
fluid mud thickness
accumulated fluid mud amount
mud thickness (m)
mud amount (×10^4 m^3)
0
0.5
1
1.5
2
2.5
50
100
150
200
250
2
4
6
8
10
12
14
16
18
20
22
24
26
28
30
32
34
36
38
40
channel segment

Fig.3

Figure 4.

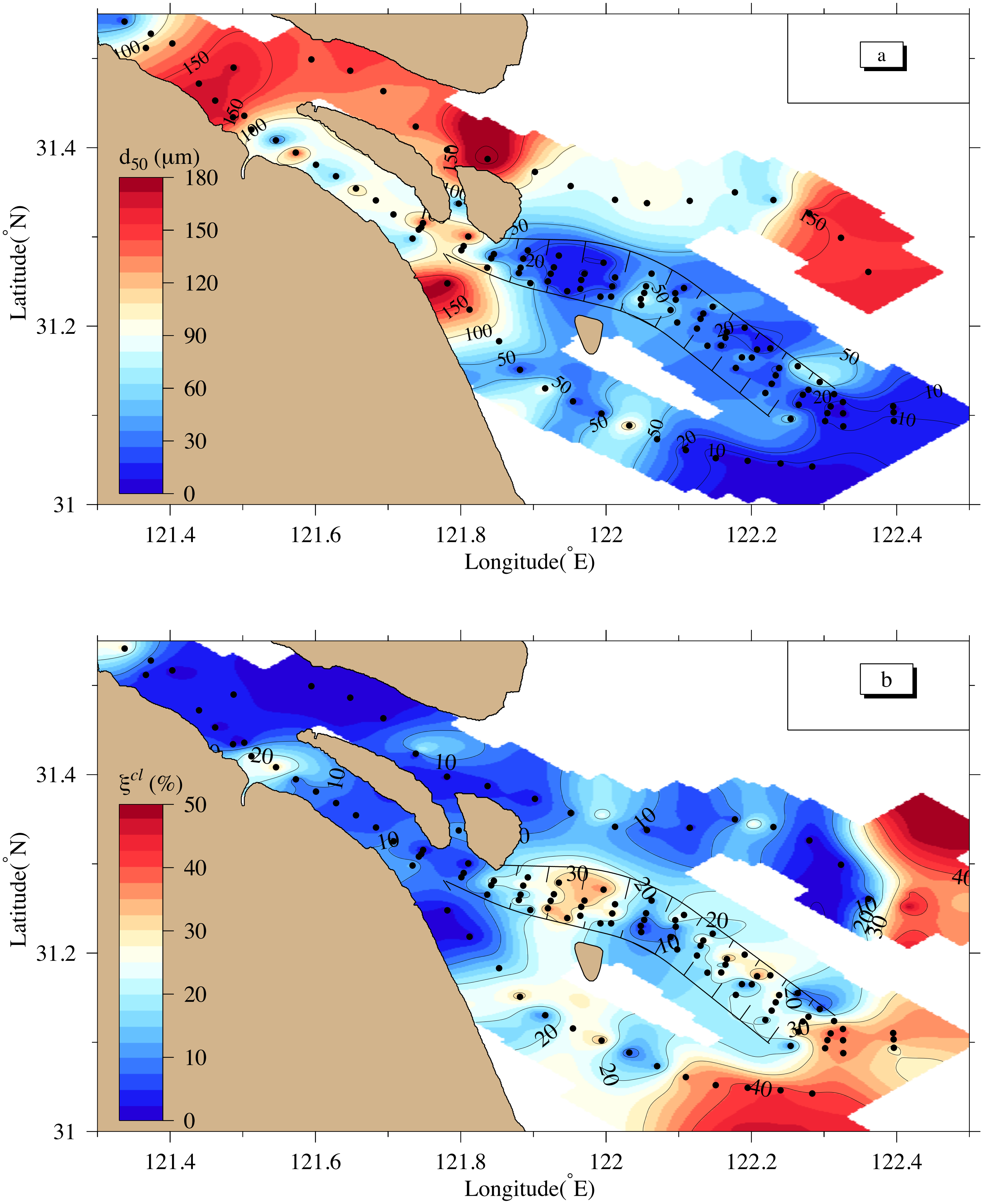
a
d50 (μm)
180
150
120
90
60
30
0
31.4
31.2
31
121.4
121.6
121.8
122
122.2
122.4
Latitude(°N)
Longitude(°E)
b
ξcl (%)
50
40
30
20
10
0
31.4
31.2
31
121.4
121.6
121.8
122
122.2
122.4
Latitude(°N)
Longitude(°E)

Fig. 4

Figure 5.

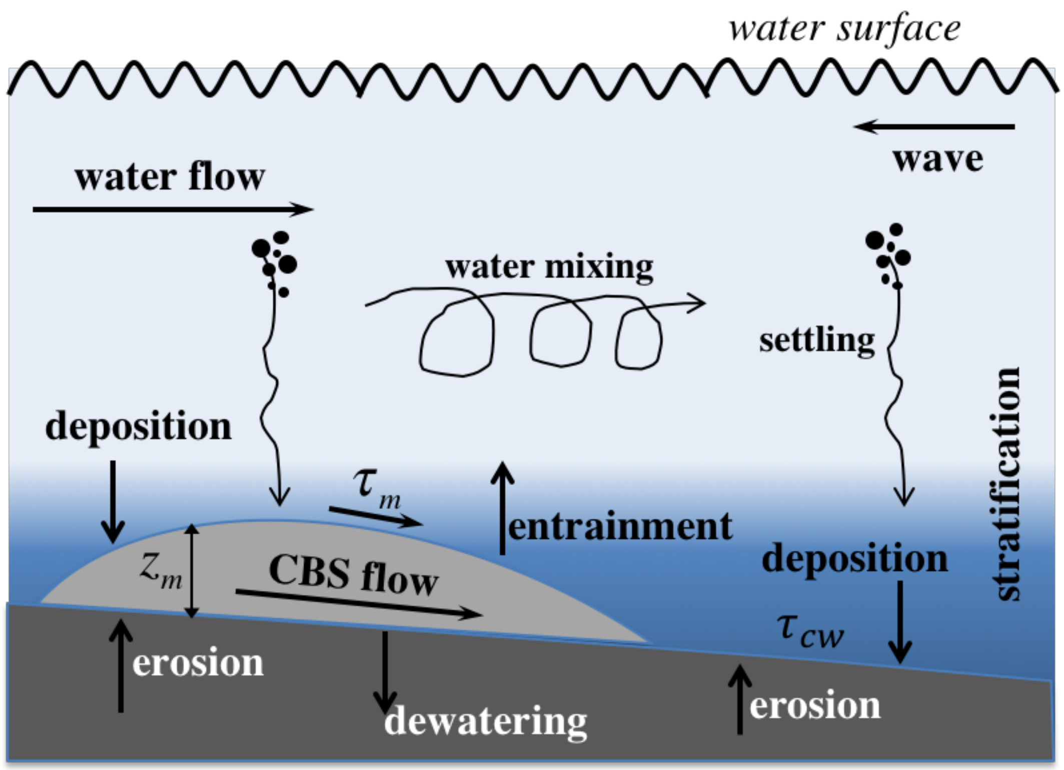
water surface
wave
water flow
water mixing
settling
deposition
stratification
τ_m
entrainment
z_m
CBS flow
deposition
τ_{cw}
erosion
dewatering
erosion

Fig. 5

Figure 6.

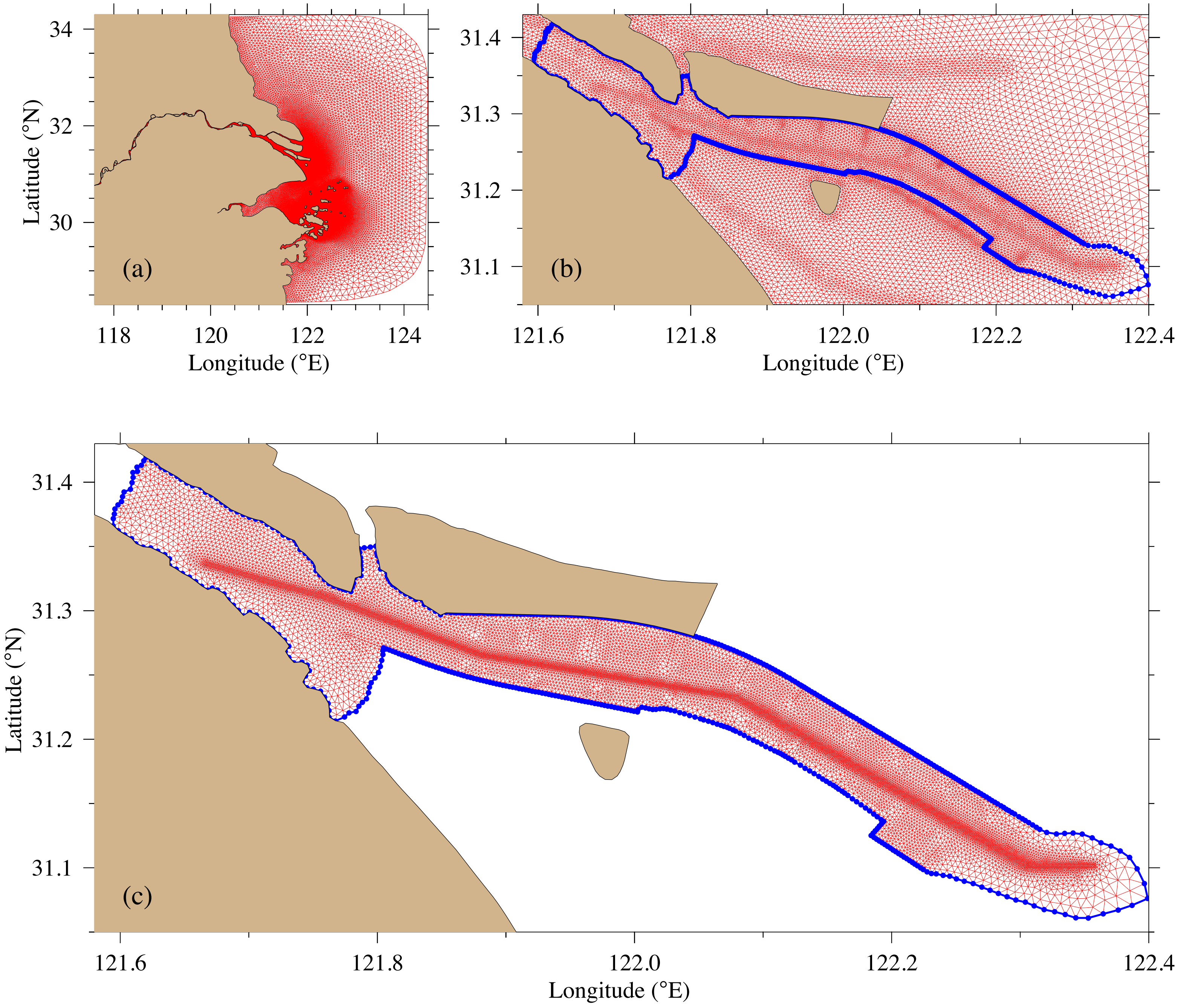
(a)
(b)
(c)
Latitude (°N)
Longitude (°E)
34
32
30
118
120
122
124
31.4
31.3
31.2
31.1
121.6
121.8
122.0
122.2
122.4

Fig.6

Figure 7.

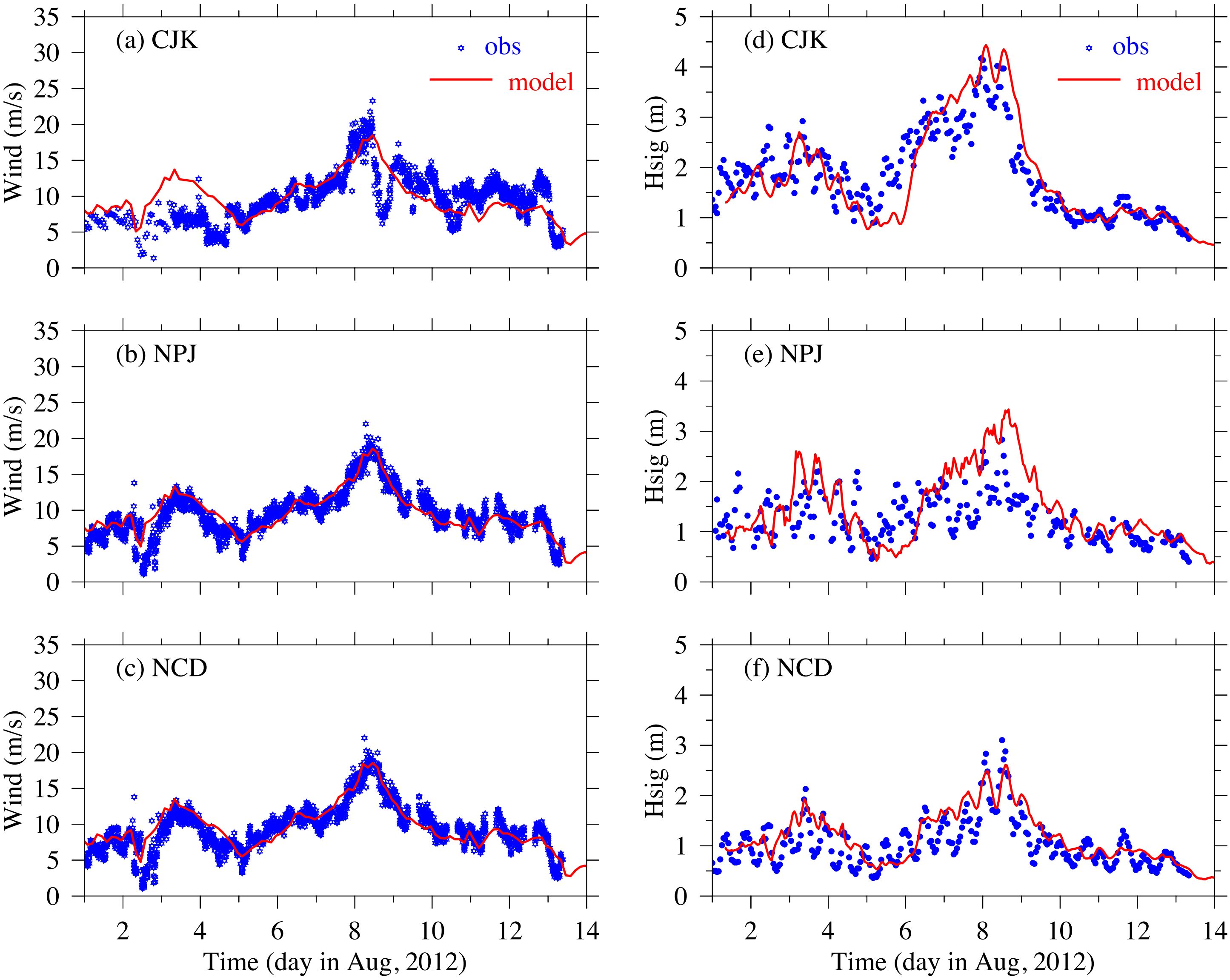

(a) CJK
obs
model
Wind (m/s)
(b) NPJ
Wind (m/s)
(c) NCD
Wind (m/s)
Time (day in Aug, 2012)
(d) CJK
obs
model
Hsig (m)
(e) NPJ
Hsig (m)
(f) NCD
Hsig (m)
Time (day in Aug, 2012)

Fig. 7

Figure 8.

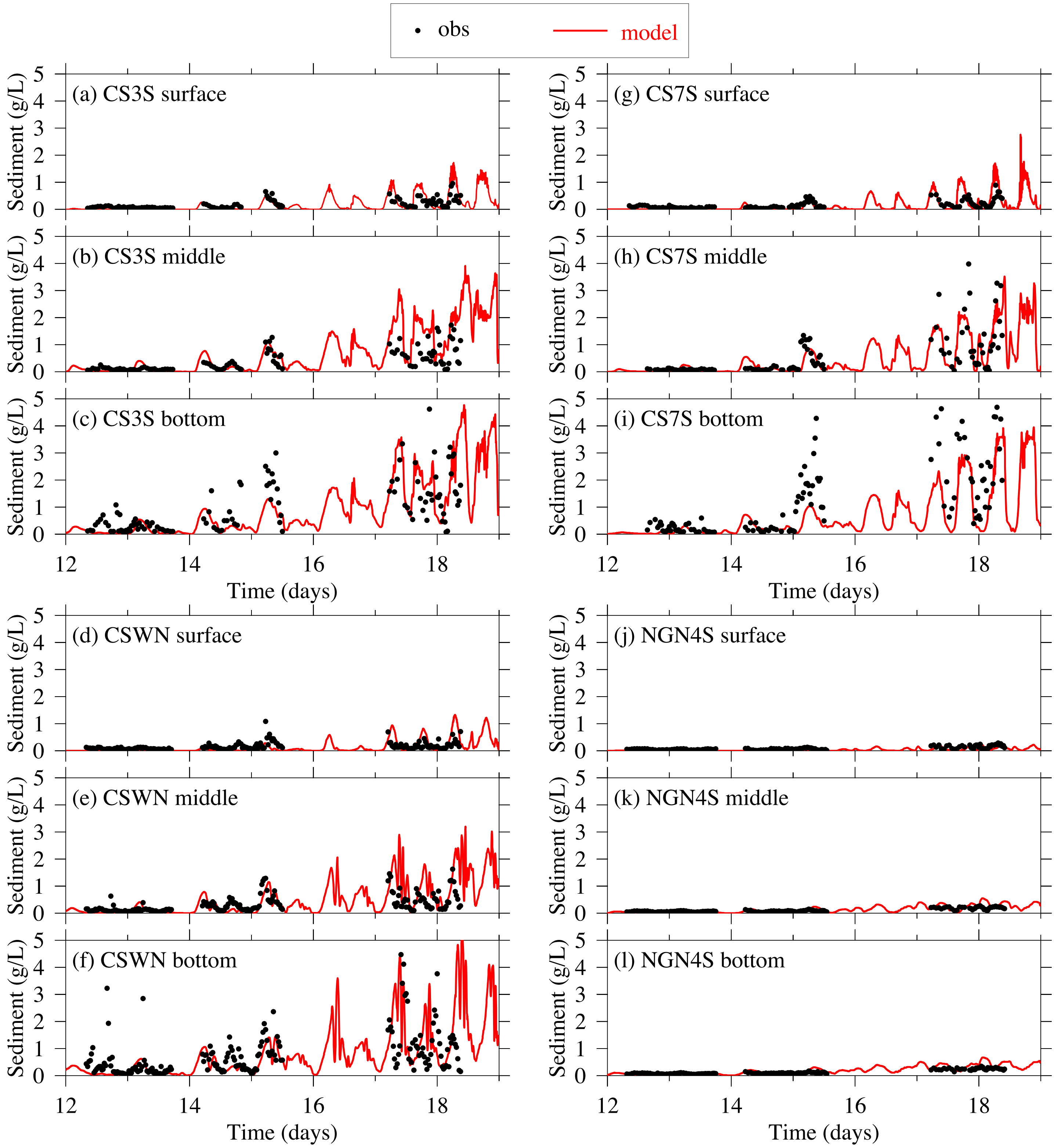

obs
model
(a) CS3S surface
(b) CS3S middle
(c) CS3S bottom
(d) CSWN surface
(e) CSWN middle
(f) CSWN bottom
(g) CS7S surface
(h) CS7S middle
(i) CS7S bottom
(j) NGN4S surface
(k) NGN4S middle
(l) NGN4S bottom
Sediment (g/L)
Time (days)
0
1
2
3
4
5
12
14
16
18

Fig. 8

Figure 9.

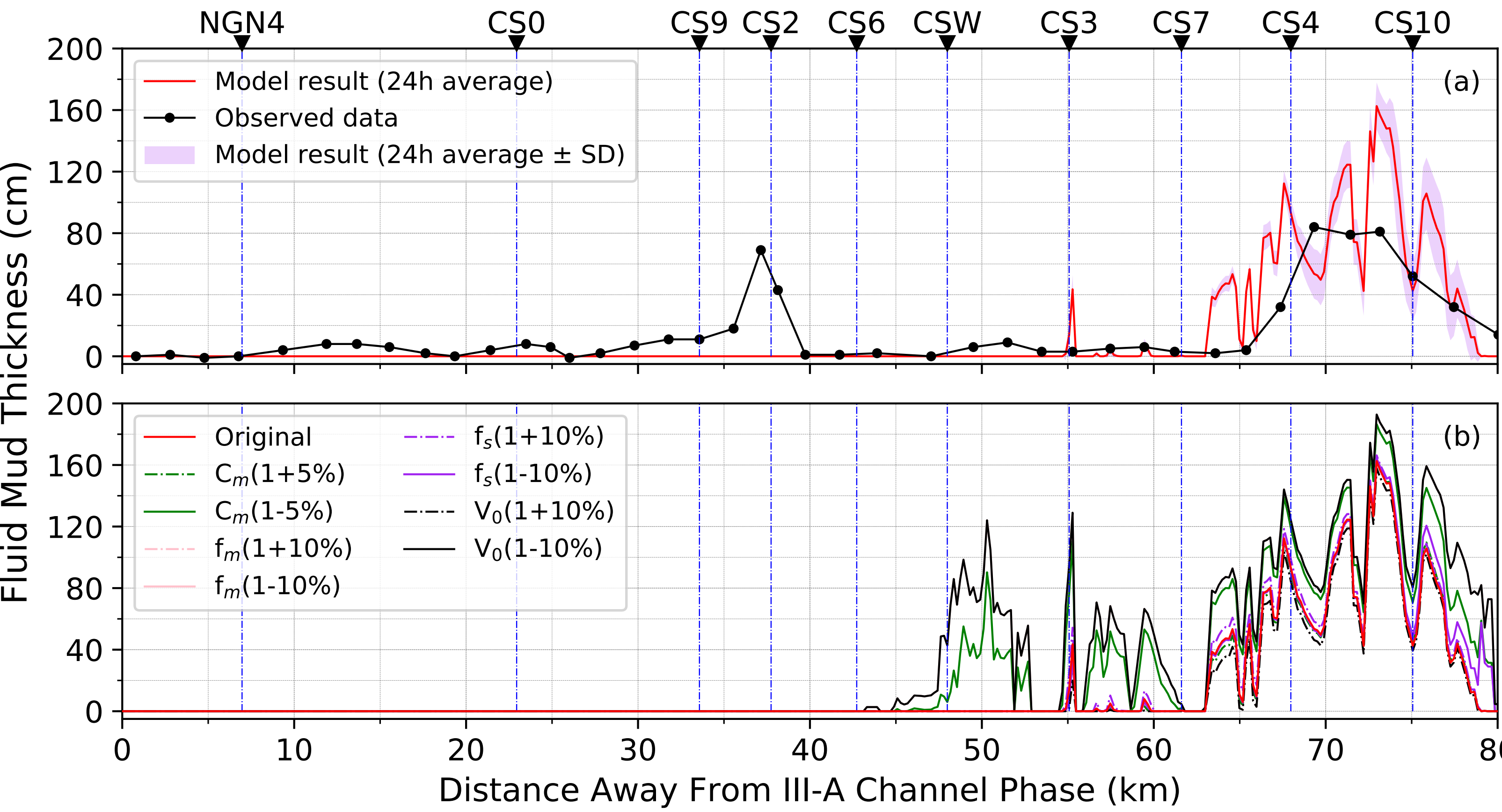

NGN4
CS0
CS9
CS2
CS6
CSW
CS3
CS7
CS4
CS10
(a)
Model result (24h average)
Observed data
Model result (24h average ± SD)
(b)
Original
C$_m$(1+5%)
C$_m$(1-5%)
f$_m$(1+10%)
f$_m$(1-10%)
f$_s$(1+10%)
f$_s$(1-10%)
V$_0$(1+10%)
V$_0$(1-10%)
Fluid Mud Thickness (cm)
Distance Away From III-A Channel Phase (km)

Fig. 9

Figure 10.

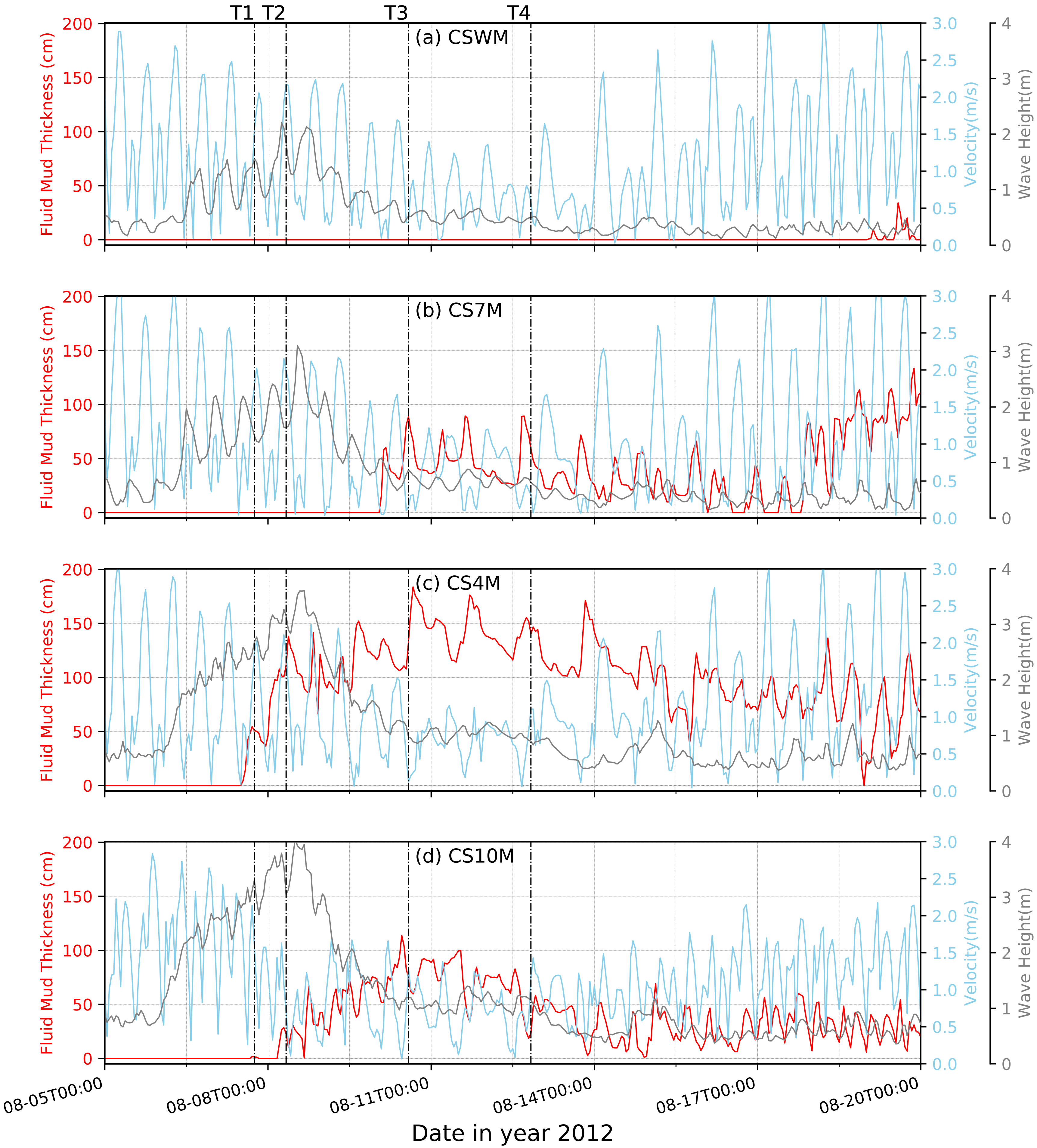

T1 T2
T3
T4
(a) CSWM
(b) CS7M
(c) CS4M
(d) CS10M
Fluid Mud Thickness (cm)
Velocity(m/s)
Wave Height(m)
08-05T00:00
08-08T00:00
08-11T00:00
08-14T00:00
08-17T00:00
08-20T00:00
Date in year 2012

Fig. 10

Figure 11.

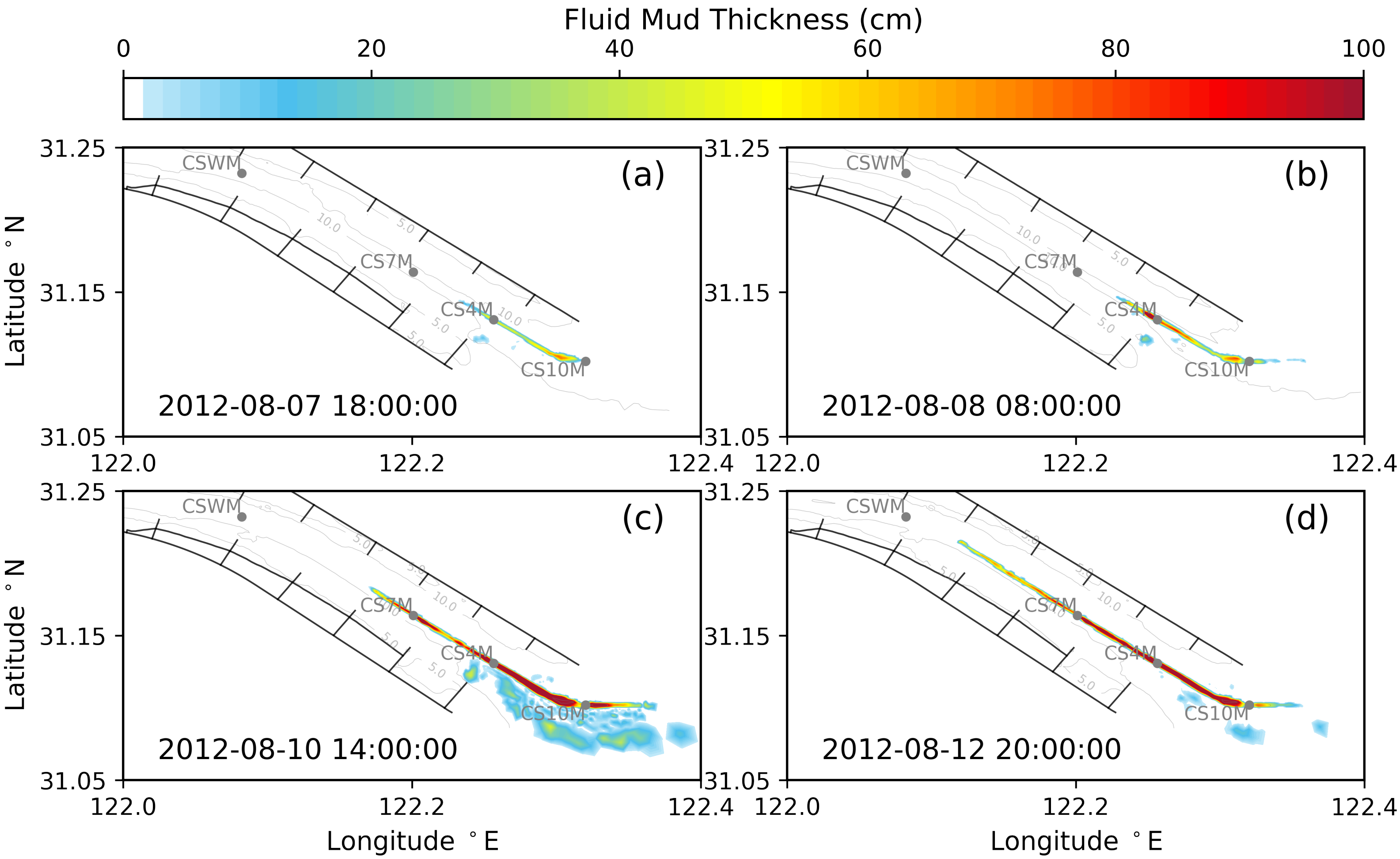
Fluid Mud Thickness (cm)
0
20
40
60
80
100
(a)
(b)
(c)
(d)
CSWM
CS7M
CS4M
CS10M
2012-08-07 18:00:00
2012-08-08 08:00:00
2012-08-10 14:00:00
2012-08-12 20:00:00
Latitude ° N
Longitude ° E
31.25
31.15
31.05
122.0
122.2
122.4

Fig. 11

Figure 12.

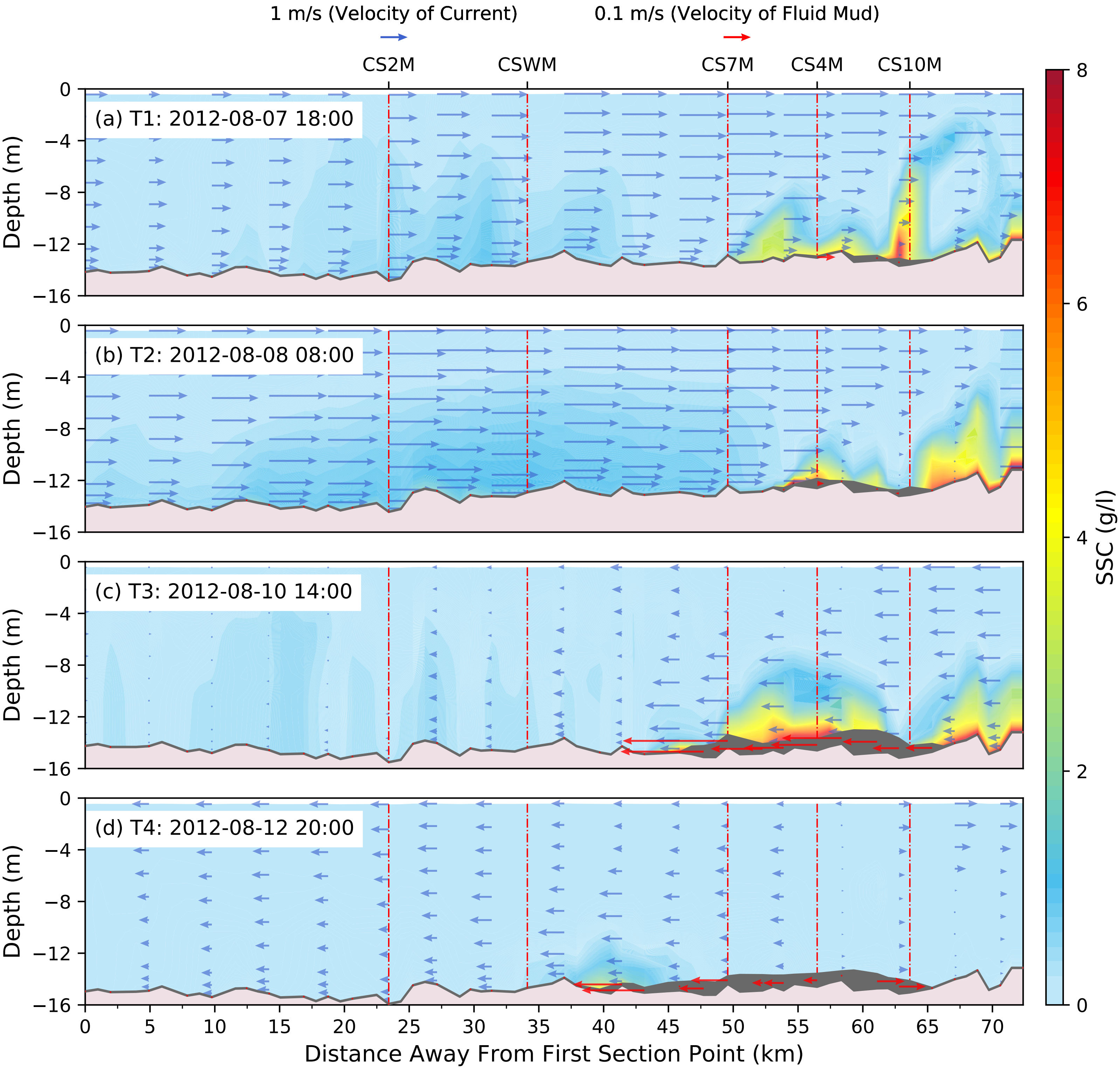

1 m/s (Velocity of Current)
0.1 m/s (Velocity of Fluid Mud)
CS2M
CSWM
CS7M
CS4M
CS10M
(a) T1: 2012-08-07 18:00
(b) T2: 2012-08-08 08:00
(c) T3: 2012-08-10 14:00
(d) T4: 2012-08-12 20:00
Depth (m)
SSC (g/l)
Distance Away From First Section Point (km)

Fig. 12

Figure 13.

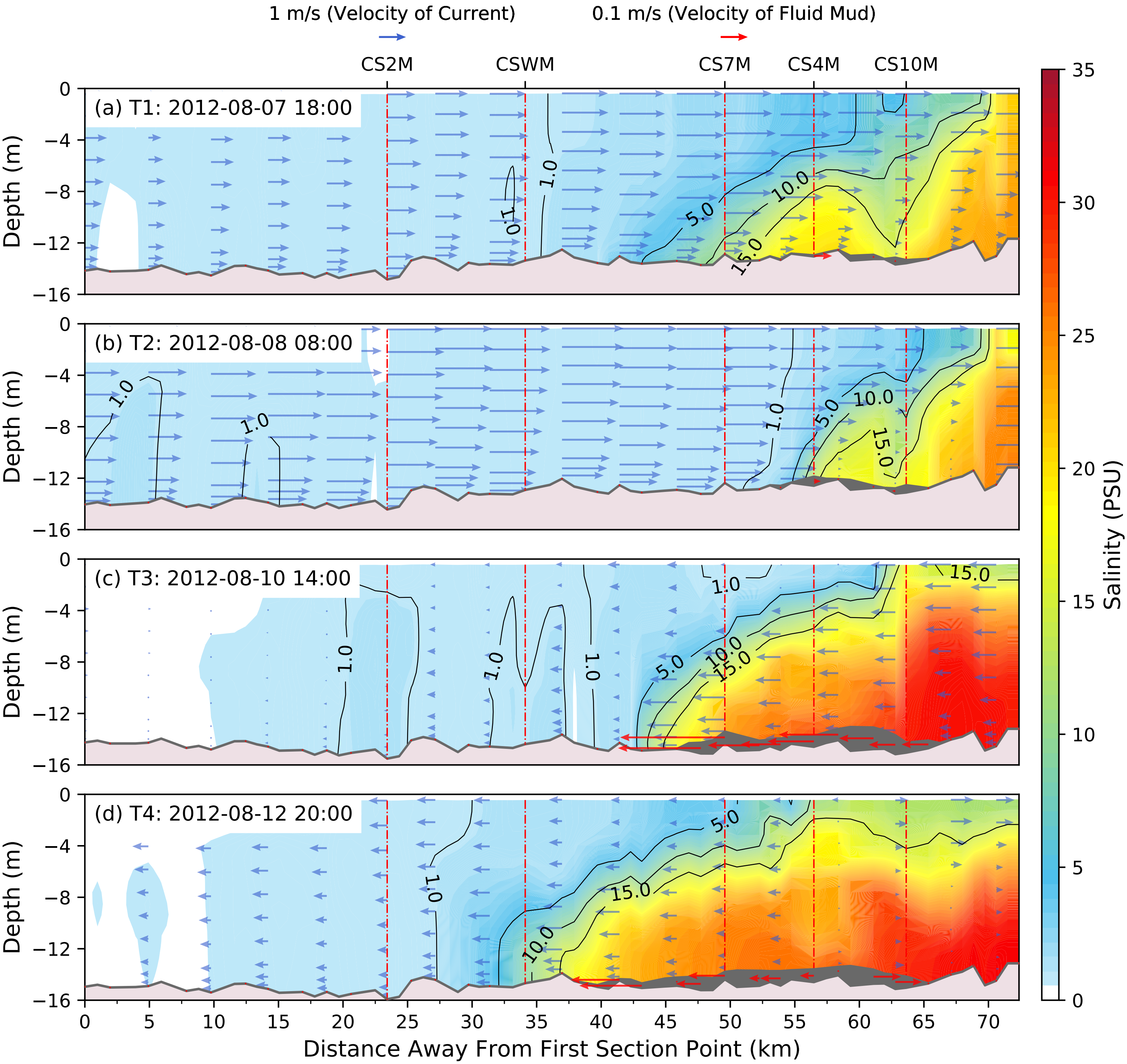
1 m/s (Velocity of Current)
0.1 m/s (Velocity of Fluid Mud)
CS2M
CSWM
CS7M
CS4M
CS10M
(a) T1: 2012-08-07 18:00
(b) T2: 2012-08-08 08:00
(c) T3: 2012-08-10 14:00
(d) T4: 2012-08-12 20:00
Depth (m)
Distance Away From First Section Point (km)
Salinity (PSU)

Fig. 13

Figure 14.

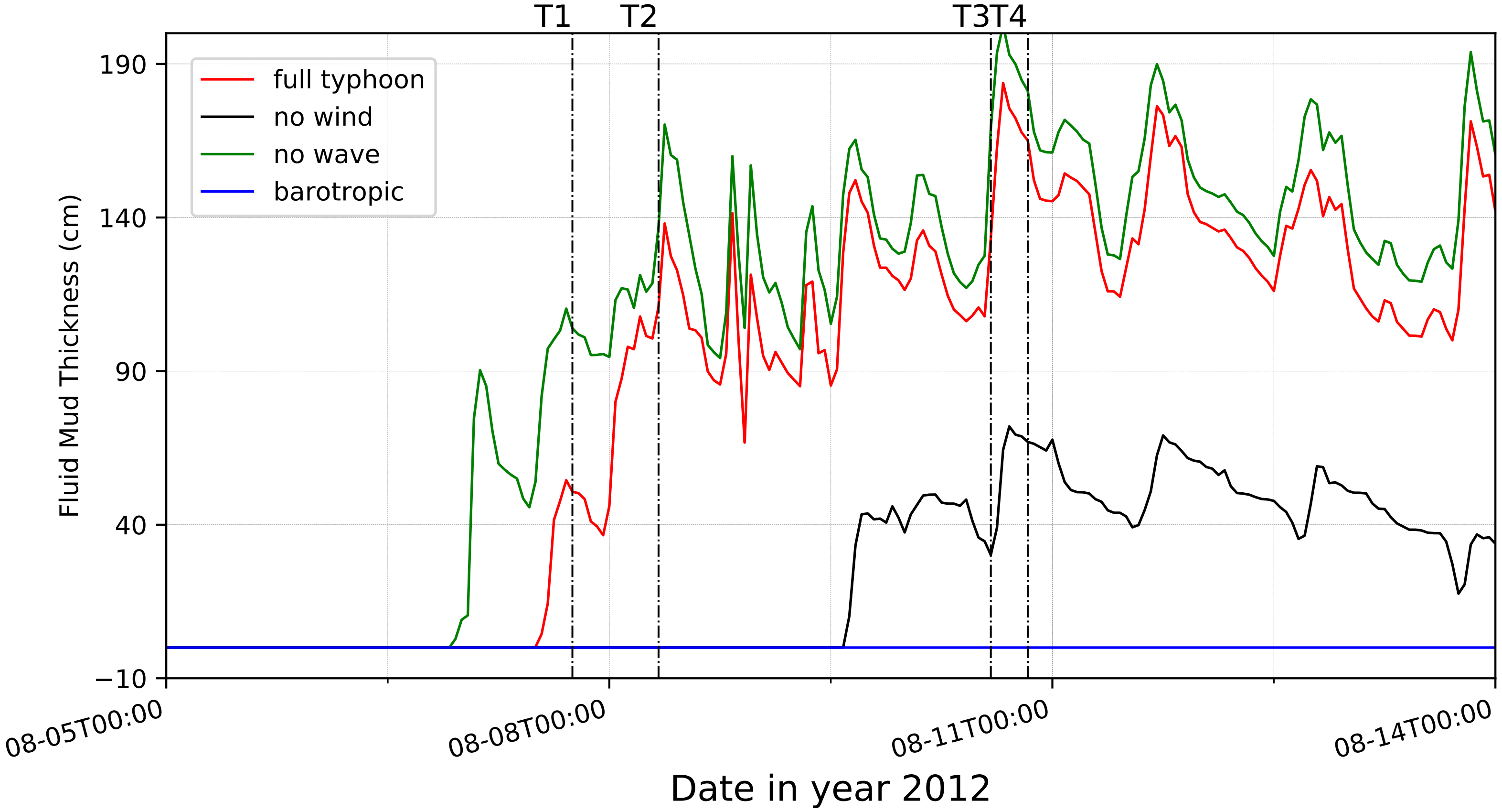

T1
T2
T3T4
190
140
90
40
−10
full typhoon
no wind
no wave
barotropic
Fluid Mud Thickness (cm)
08-05T00:00
08-08T00:00
08-11T00:00
08-14T00:00
Date in year 2012

Fig. 14

Figure 15.

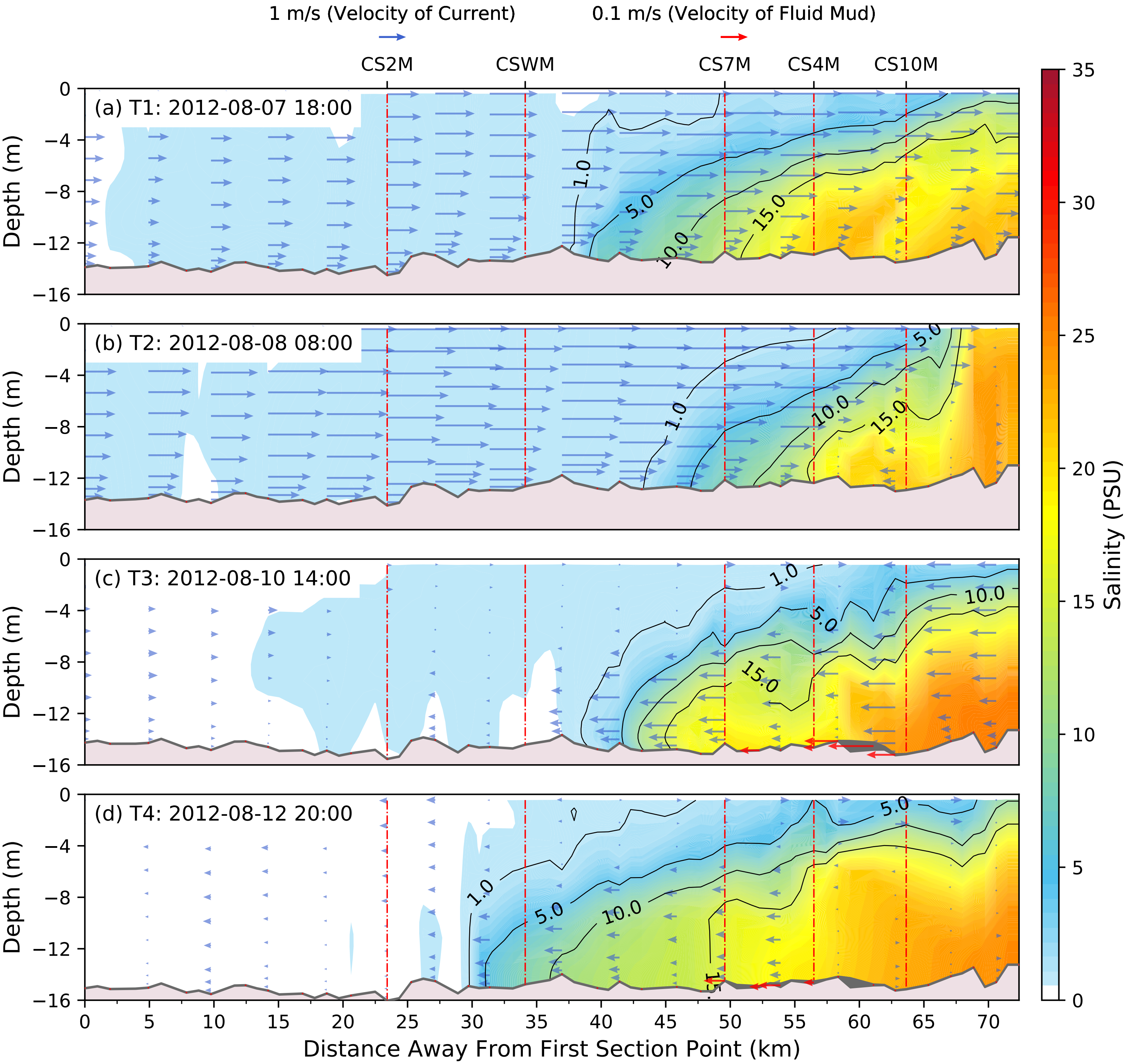
1 m/s (Velocity of Current)
0.1 m/s (Velocity of Fluid Mud)
CS2M
CSWM
CS7M
CS4M
CS10M
(a) T1: 2012-08-07 18:00
(b) T2: 2012-08-08 08:00
(c) T3: 2012-08-10 14:00
(d) T4: 2012-08-12 20:00
Depth (m)
Distance Away From First Section Point (km)
Salinity (PSU)

Fig. 15

Figure 16.

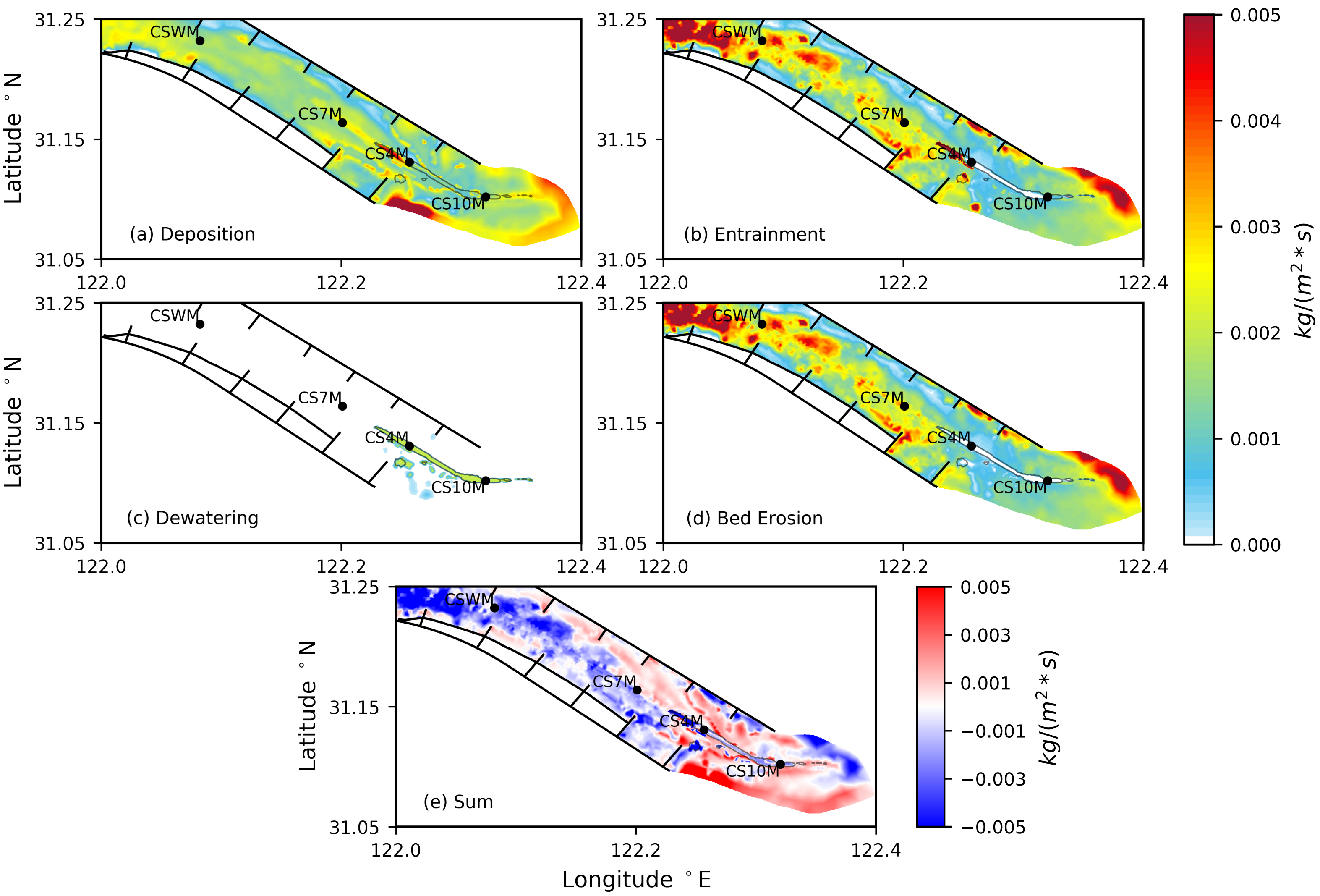
(a) Deposition
(b) Entrainment
(c) Dewatering
(d) Bed Erosion
(e) Sum
CSWM
CS7M
CS4M
CS10M
Latitude °N
Longitude °E
31.25
31.15
31.05
122.0
122.2
122.4
kg/(m^2*s)
0.005
0.004
0.003
0.002
0.001
0.000
−0.001
−0.003
−0.005

Fig. 16

Figure 17.

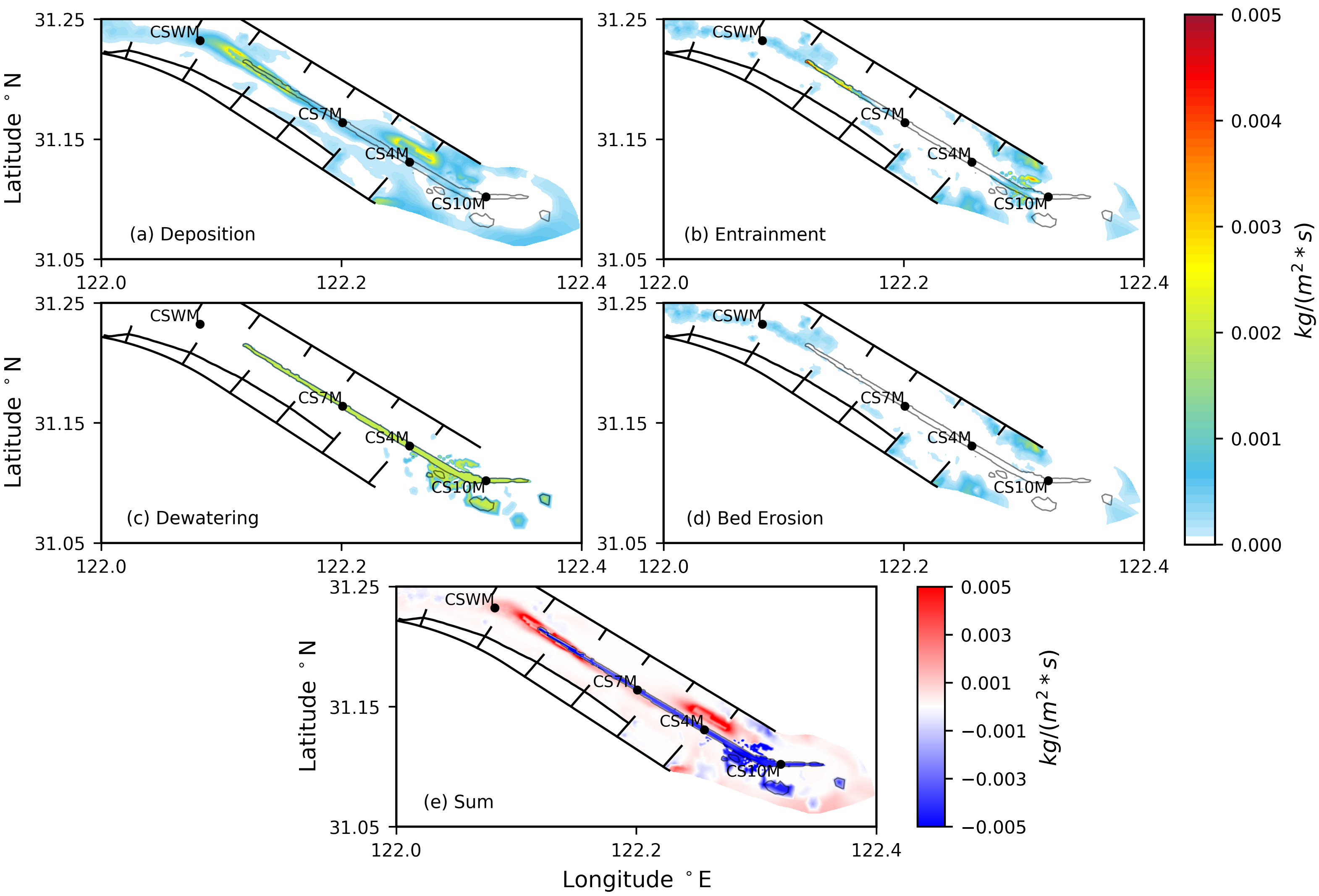
(a) Deposition
(b) Entrainment
(c) Dewatering
(d) Bed Erosion
(e) Sum
CSWM
CS7M
CS4M
CS10M
Latitude °N
Longitude °E
31.25
31.15
31.05
122.0
122.2
122.4
$kg/(m^2*s)$
0.005
0.004
0.003
0.002
0.001
0.000
−0.001
−0.003
−0.005

Fig. 17